

A MOBILE ENABLED MICRO COMMUNICATION DEVICE FOR BIOSENSING

A Thesis by

Phanikumar Vuka

Bachelor of Technology, SRM University, India, 2013

Submitted to the Department of Electrical Engineering and Computer Science
and the faculty of the Graduate School of
Wichita State University
in partial fulfillment of
the requirements for the degree of
Master of Science

December 2017

© Copyright 2017 by PhanikumarVuka
All Rights Reserved

A MOBILE ENABLED MICRO COMMUNICATION DEVICE FOR BIOSENSING

The following faculty members have examined the final copy of this thesis for form and content, and recommend that it be accepted in partial fulfillment of the requirement for the degree of Master of Science with a major in Electrical Engineering.

Ali Eslami, Committee Chair

Yanwu Ding, Committee Member

Davood Askari, Committee Member

DEDICATION

To my parents, my sisters.

Life's is not about how hard of a hit you can give...it's about how many you can take and still keep moving forward.

ACKNOWLEDGMENTS

I would like to thank my advisor, Prof Ali Eslami, for his support and valuable comments throughout the time of my Master's degree research. His guidance and patience made it possible for me to develop this thesis. I am also grateful to my committee members for generously taking the time to evaluate my thesis.

I am very thankful to Professor Preetika Kumar, for her encouraging words to boost my confidence, and my colleague Ali Behfarnia, for his support in my research. My appreciation also goes out to all my friends in Wichita, particularly Kaushik Jeevarathnam, Arun Kaarthick, and Nikhil Chakravarthy, for their endless support and care when I needed it.

This thesis is dedicated to my parents for all their sacrifices, endless love and support along the way. I am also thankful for the support of my siblings.

ABSTRACT

In the recent decade, the e-health care industry has seen a rapid growth in state-of-the-art advancement in many related fields. The ability of biosensors to stimulate and continuously monitor vital organs has proven to be helpful for various medical conditions ranging from seizures to cancer. To build devices with such capabilities, challenges in various domains, such as biocompatible materials, low-power wireless communication, processing, and sensing techniques, must be solved. Most of the proposed device models have used a single energy source for powering and communication, without the implementation of error-correction/detection techniques, thus limiting the communication range to millimeters. This work proposes a bio-mote, a model of a communication device that can circulate inside the human body and communicate with a wearable or handheld device such as a cell phone. The proposed model has integrated low-power modulation, powering, and error-correction techniques in order to communicate with an external device that is placed at a distance in the centimeter range. Assuming the human body to be an additive white Gaussian noise (AWGN) channel and with an implant coil radius of 30 μm , performance of the proposed model has been analyzed using MATLAB. A maximum communication range of 5 cm with a bit error rate (BER) of 0.0001 has been achieved.

TABLE OF CONTENTS

Chapter	Page
1. INTRODUCTION.....	1
1.1 Motivation	1
1.2 Problem Description	2
1.3 Contribution.....	2
1.4 Organization	2
2. LITERATURE REVIEW	4
2.1 Powering.....	4
2.1.1 Energy Harvesting	6
2.1.2 Optical.....	7
2.1.3 Ultrasound.....	8
2.1.4 Radio Frequency	13
2.1.5 Terahertz	17
2.2 Communication.....	17
2.2.1 Modulation.....	17
2.2.2 Performance Measure	18
3. PROPOSED SYSTEM AND RELATED PARAMETERS.....	20
3.1 Proposed System.....	20
3.2 Inductive Coupling Parameters.....	22
3.2.1 Mutual Induction	23
3.2.2 Induced Voltage	24
3.2.3 Direct Current Resistance	24
3.2.4 Alternating Current Resistance	25
3.2.5 Skin Effect	25
3.2.6 Parasitic Capacitance	26
3.3 Ultrasound Parameters	26
3.3.1 Size and Frequency Trade-Off.....	27
3.3.2 Attenuation.....	27
3.3.3 Reflection.....	29
3.4 Modulation and Related Parameters	31
3.4.1 ASK	32
3.4.2 BPSK	33
3.5 Error-Correction Coding and Related Parameters	34
3.5.1 Reed-Solomon Codes	35
3.5.2 Hamming Codes.....	36

TABLE OF CONTENTS (continued)

Chapter	Page
4. MODELING OF PROPOSED SYSTEM.....	39
4.1 Magnetic Induction Communication Model.....	39
4.2 Ultrasound Powering Model.....	42
5. RESULTS	46
5.1 Introduction	46
5.2 Voltage Induced.....	46
5.3 Power Induced	47
5.4 Bit Error Rate Using Error-Correction and Modulation	
5.4.1 Comparison of BPSK Using Hamming vs BPSK Using RS Codes	47
5.4.2 Comparison of ASK Using Hamming vs ASK Using RS Codes	48
5.5 Conclusion.....	49
REFERENCES	52

LIST OF TABLES

Table	Page
1. Electromagnetic Field Properties in Different Human Tissues	15
2. State-of-the-Art in Low-Power, Low-Area Modulation in Terms of Performance Measure.....	19
3. List of Attenuation Coefficients and Velocity of Acoustic Waves in Various Tissues.....	30
4. Acoustic Impedance of Different Body Tissues	31
5. Amount of Energy Reflected When Ultrasound Passes through Various Interfaces.....	32
6. Different Parameter Values Assumed in Order to Calculate Performance of Proposed System.....	46

LIST OF FIGURES

Figure	Page
1. Range of power consumption required by applications of various scales	5
2. Approaches toward powering of bioimplants.....	6
3. Electromagnetic spectrum.....	13
4. Near-field and far-field radiation of a coil.....	14
5. Bio-mote with inductive coil and biosensor	21
6. Cell phone (reader) powering on and communicating with motes in read zone.....	21
7. Complete block diagram of the process involved in proposed system.....	22
8. Inductance model in terms of RLC	26
9. Attenuation over various distances and operating frequencies	27
10. Amplitude shift keying.....	33
11. Phase shift keying	34
12. Implementation of RS (7, 3) using shift registers	37
13. Modeling of the channel for MI	39
14. Nanogenerator using ZnO nanowires and rectifying circuit that can store energy in capacitor (top) and its equivalent model (bottom)	43
12. Comparison between actual device and mode by measuring amount of voltage generated as function of number cycles of ultrasound	46
13. Voltage induced in external coil due to bio-mote with respect to distance separating bio-mote and external coil (mobile phone) power induced	47
14. Power induced in external coil due to bio-mote with respect to distance separating bio-mote and external coil (mobile phone).....	47
15. BER for various distances between external device and bio-mote using BPSK modulation	48

LIST OF FIGURES (continued)

Figure	Page
16. BER for various distances between external device and bio-mote using ASK modulation	49

LIST OF ABBREVIATIONS

AC	Alternating Current
ASK	Amplitude-Shift Keying
AWGN	Additive White Gaussian Noise
BER	Bit Error Rate
BMI	Brain-Machine Interface
BPSK	Binary Phase-Shift Keying
CMOS	Complementary Metal Oxide Semiconductor
CUT	Capacitive Ultrasonic Transducer
DC	Direct Current
DFSK	Distributed Frequency-Shift Keying
FDA	Food and Drug Administration
FSK	Frequency-Shift Keying
IMD	Implantable Medical Device
ISM	Industrial, Scientific, and Medical Radio Band
LED	Light-Emitting Diode
LOS	Line-of-Sight
MI	Magnetic Induction
NFC	Near-Field Communication
OOK	On-Off Keying
PSC	Printed Spiral Coil
PSK	Phase-Shift Keying
PT	Physiotherapy

LIST OF ABBREVIATIONS (continued)

PTE	Power Transfer Efficiency
PV	Photovoltaic
PVDF	Piezoelectric Polyvinylidene Fluoride
PZT	Piezoelectric Transducer
QCPSK	Quasi-Coherent Phase-Shift Keying
RF	Radio Frequency
RFID	Radio Frequency Identification
RS	Reed-Solomon (Codes)
SNR	Signal-to-Noise Ratio
UTET	Ultrasonic Transcutaneous Energy Transfer
VCSEL	Vertical Cavity Surface-Emitting Laser
WPT	Wireless Power Transfer

LIST OF SYMBOLS

α	Angle of Arrival of Signal
μ	Magnetic Permeability
B_0	Strength of Arrival Signal
c	Velocity of Light
E_b	Bit Energy
f_r	Resonance Frequency
G	Generator Matrix
H	Parity Check Matrix
M	Mutual Inductance
$m\%$	Modulation Index
P_r	Power Received
PL	Path Loss
P_b	Probability of Error
Q	Quality Factor of Circuit
R_L	Load Resistance
R	Distance between External Coil and Bio-Mote
t	Number of Errors Corrected
Z	Impedance

CHAPTER 1

INTRODUCTION

1.1 Motivation

Imagine if you could monitor the function of your vital organs in real time on your cell phone, by measuring their temperature, concentration of glucose, oxygen, and other chemicals. Cell phones have access to servers with tremendous processing power and memory, capable of analyzing very large amounts of data in a very short time and looking for abnormalities. If these capacities could be utilized, the physician and laboratory both could be brought to your cell phone. Cancer tumors could be detected in an early stage when the chance of survival is high, heart attacks could be avoided by early alerts, and so on. The key to this new era of health care is the production of tiny devices that can take measurements inside the body and communicate that information to our cell phones or wearable devices. Such devices are also the gateway to nanomedicine by enabling nanorobots and smart drug delivery, among others.

Most papers have proposed to implement a network of such small devices in the body. But in order to implement a network, each of these devices should have the capability of implementing networking protocols, which demand that the devices have processing and storage capabilities. It is not feasible to fulfill these demands with the limited amount of power available using the present state-of-the-art implantable medical device (IMD) semiconductor. It is not rational to implement a network of sensors if an individual sensor does not possess such a capability. Despite the tremendous effort in nanocommunications and miniaturized medical implants, we are still far from designing such devices, even in microscale.

All of this provides the motivation to further investigate various approaches in order to achieve miniaturized medical implants that can individually sense and communicate, rather than

a network with an external device that could also help in taking a step further in realizing the implementation of a network of sensors.

1.2 Problem Description

In the literature, the communication range of most IMDs is limited to a few millimeters, which is not sufficient for deep-tissue measurements. The work in this thesis focuses on improving the communication range from millimeters to centimeters on a microscale implementation.

1.3 Contribution

The main aim of this paper is to achieve a communication distance in the range of a few centimeters. The main contributions of the paper are as follows

- Proposal for a hybrid powering and communication model called a bio-mote, a device that can communicate in the range of few centimeters.
- Inclusion of error-control coding on the bio-mote to improve performance.
- Performance comparison of different error-coding and modulation techniques:
 - Amplitude-shift keying (ASK) and Hamming code (15, 11)
 - ASK and Reed-Solomon (RS) codes (31, 26)
 - Binary phase-shift keying (BPSK) and Hamming code (15, 11)
 - BPSK and RS codes (31, 26)

1.4 Organization

This paper is organized as follows: Chapter 2 provides a brief overview and literature review on various techniques of powering and communication systems. Chapter 3 explains the proposed system and related parameters. Here, a hybrid system for powering and communication is proposed, and the parameters related to analyze the build blocks involved in the proposed

system are explained in detail. Chapter 4 discusses in detail the modeling and analysis of the proposed ultrasound system used for powering and the Magnetic Induction (MI) for communication. In Chapter 5, the proposed system is modeled in MALAB to evaluate its performance.

CHAPTER 2

LITERATURE REVIEW

The main aspects of any implantable communication device are powering, communication, and sensing. Various techniques that have been adopted in order to power an implantable device wirelessly and communicate with an external device are presented in this chapter. Most techniques discussed below can be used for both powering as well as communication.

2.1 Powering

Following the conception of “smart dust” or “mote” [1], a major hurdle in implementing these devices was the size of the required power source. While the technology node in semiconductor fabrication has decreased more than 20 times since then, the battery technology has not shared the same miniaturization rate. However, since space is so precious on an implantable medical device, it would be advantageous if the battery or piezo-electric component could be removed all together and the IMD could be designed as a passive device powered on from the outside only.

For this purpose, external powering through ultrasound or magnetic induction are the most extensively studied and implemented methods for both communication and powering interchangeably. Individually these methods have advantages and disadvantages depending upon the purpose (powering or communication) and the medium (air or water) in which they are working. Figure 1 shows a range of power consumption required by applications of various scales.

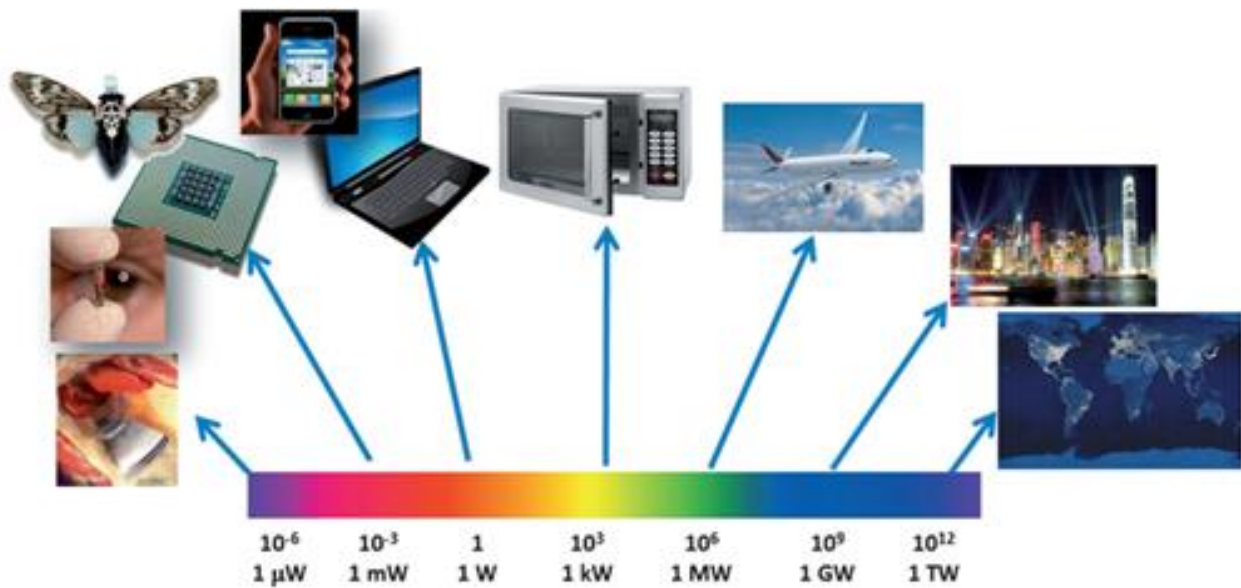


Figure 1. Range of power consumption required by applications of various scales [2].

Power is the most important factor of an implantable device, since the amount of it available determines the capabilities. For most IMD's the power requirement would be a range between μ W to mW. Different approaches to powering bioimplants taken up in the literature are shown in Figure 2. The most traditional approach is batteries. Conversion of chemical energy to electrical energy can be done using micro bio-fuel cells (using glucose), similar to the concept of daily-usage batteries.

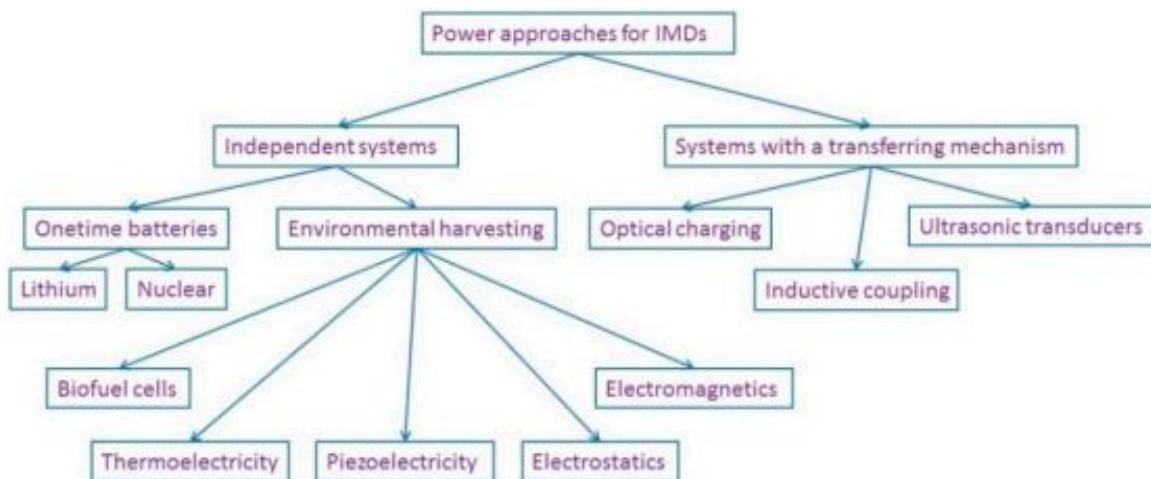


Figure 2. Approaches towards powering bioimplants [3].

The main disadvantage of using a battery in an IMD is its lifespan, since it is very difficult to replace once inserted inside the body. The toxic nature of battery materials is also a concern. The limited life span and toxicity makes the battery a less attractive option as a primary power source. Therefore, alternative techniques for energizing implantable micro devices are needed. The two major approaches taken in the literature are energy harvesting and wireless powering.

2.1.1 Energy Harvesting

Energy-harvesting techniques in order to utilize various forms of energy, such as solar, wind, etc., to generate power for applications that have very large energy requirements have been evolving in recent years. Similarly, the human body is the source of various forms of energy: chemical, kinetic, heat, etc. The available power that has been evaluated from various human activities is as follows: 1 W for breathing, 0.93 W from blood pressure, 35 W from upper-limb motion, and 67 W from walking at the rate of two steps per second [4], which is more than enough to power an IMD with power requirements that are significantly below these numbers. Energy-harvesting techniques have become an attractive alternative source to running low-power biomedical implants, and these techniques have gained considerable attention in recent years [5]. Various IMDs have been studied and tested in order to harvest a part of the energy that is produced in the human body. Techniques such as nanoenergy harvesting with today's state-of-the-art research requires an area of a few mm² to provide only 1 μW [6, 7]. Harvested piezoelectric energy could potentially power active IMDs [8]. When placed in a blood vessel, a piezoelectric device can translate the mechanical energy of blood pressure to electrical energy. Various other forms of chemical, thermal, electrostatic, and mechanical energy can also be harvested from the human body [9]. Despite promising advantages from

results in this field, the present state of the art in energy harvesting inside the human body is not mature enough and reliable for powering an IMD [10, 11, 12, 5]. Every form of energy harvesting has its own limitations; for example, harvesting through piezoelectricity is limited to a very few locations inside the human body, such as temperature-based harvesting (thermal) produces very minimal output, etc. [13]. Energy harvesting from the human body is typically more difficult than energy harvesting in the industrial environment primarily due to the size constraint [5].

2.1.2 Optical

Optical-based devices operate in the infrared or near-infrared region [14] and can be used as a source of both powering and communication. The major advantage of using optical-based devices for IMD is their ability to be minimized without compromising the efficiency of the device, which is not the case with ultrasound, or inductive-based powering. [15, 16, 17]. Photovoltaic (PV) cells and light-emitting diodes (LEDs) are the generally used transducers for optical-based charging and communication. In the work of Aktan et al. [18], a practical design of a microsystem has been demonstrated, by aligning an on-chip PV cell with the tip of an optical fiber for powering and a separate laser diode for communication. In the work of Haydaroglu and Mutlu [19], a PV cell was replaced by an LED, due to its efficiency in that it can be used for both communication and energy harvesting and has been integrated to an ASIC of dimensions $350 \times 350 \mu\text{m}^2$, $230 \times 210 \mu\text{m}^2$. Ayazian and Hassibi [20] used PV cells with dimensions in mm^2 as transducers to generate power using the ambient light passing through tissue. With their design, they were able to harvest power in the range of a few μW 's of power in bright light conditions with a 40-dB optical loss. An energy-autonomous and fully integrated complementary metal oxide semiconductor (CMOS) implantable sensor of dimensions $2.5 \times 2.5 \text{mm}^2$ has also been

demonstrated [21], with the capability of harvesting a few μW 's of energy using PVcells using the ambient light passing through tissues and polarized electrodes for communication. An optically powered single-channel retinal implant was developed and tested for epi-retinal stimulation using micromachining techniques [22]. When activated by short impulses of infrared light, these implants could generate a current of $100 \mu\text{A}$. Radio frequency (RF) tags with on-chip silicon photodiodes of miniaturized dimensions of $500 \times 500 \mu\text{m}^2$ sizes were powered using a laser beam of RF tags [23]. Mujeeb-U-Rahman et al. [24] demonstrated and validated N-well-based CMOS-integrated PV devices to harvest optical energy when concentrated laser light was used as the power source. Furthermore, optical-based data communication was demonstrated on the same platform using an ultra-small vertical cavity surface-emitting laser (VCSEL) through the same platform. Stacked and individual voltage recordings of up to 1.2 V at a distance of 3 mm in tissues were observed using N-well-based CMOS photodiodes of dimensions $30 \mu\text{m} \times 30 \mu\text{m}$, $100 \mu\text{m} \times 100 \mu\text{m}$, and $500 \mu\text{m} \times 500 \mu\text{m}$. In most of these studies, the major advantage is the ability to miniaturize the device that can harvest optical energy at microscale. The major disadvantage is that the optical source must be focused and concentrated in order to achieve an adequate amount of power, which is not always possible when numerous sensors are placed in the body for monitoring. In most cases, the source of powering is a laser, the irradiation of which could raise the skin temperature. Because optical devices operate in the higher frequency spectrum, the power loss is high.

2.1.3 Ultrasound

Ultrasound consists of acoustic waves with a frequency of more than 20,000 cycles per second. It can be used as a source of both powering and communication. Acoustic waves are vibrations of molecules or atoms of the propagation medium. These vibrations are organized in a

sinusoidal fashion. Acoustic waves are the transmission technology of choice for underwater communications, since they are known to propagate better than their RF counterpart in a medium composed mainly of water [25, 26, 27]. Acoustic waves typically belong to a frequency range between 0 and 100 kHz, and have been successfully used for underwater communications since World War II [28]. Ultrasound has the advantage when compared to its counterpart radio frequency, due to its lower speed in human tissue (1500–200m/s) and much smaller wavelengths, which help in implementing more directional transmitters and receivers at lower frequencies [29], their immunity towards electromagnetic radiation, lower absorption in human tissues when compared to RF which gets absorbed significantly. Attenuation of ultrasonic waves operating at 1 Mhz for a distance over a 10–20 cm link is in the range of 10–20 dB, whereas attenuation for RF waves operating at 2.4 Ghz in the industrial, scientific, and medical (ISM) radio band is in the range of 75–130 dB [30].

On average, 65% of the human body consists of water. The Food and Drug Administration (FDA) allows an intensity of 7.2 mW/mm for diagnostic ultrasound applications [33], which is about two orders of magnitude higher than the safe RF exposure limit in the body (10–100 W/mm [32, 33]). Consequently, ultrasound is used for various medical purposes. Many medical imaging techniques use ultrasound for non-invasive diagnosis applications in which the echo of the transmitted ultrasound is analyzed to create an image of the target applications such as examining fetus development in women, scanning for tumors in breast cancer patients, and employing physiotherapy (PT) for purposes of producing heat in tissues [34, 35]. This widespread use for imaging and medical purposes has led to the development of various types of ultrasound transducers. An ultrasound transducer is a device that can convert an AC signal into

ultrasound and vice versa. Medical imaging primarily uses ultrasound in frequencies ranging between 3 and 6 MHz.

The advantage to better propagating in water than any other waves (RF, optics) (i.e., acoustic waves at non-audible frequencies, above 20 kHz) makes ultrasound feasible to provide support for both communication and powering in the human body. Ultrasound has been studied to power IMDs [36, 37, 38, 39, 40, 41]. In the work of Charthad et al. [42], ultrasound was used to power an implant with a transducer 1.4 mm thick and 1 mm in diameter. Here, power of 100 μ W was successfully delivered at 3 cm using a commercial transmitter operating at a frequency of 1 Mhz. In the work of Meng and Kiani [43], an ultrasonic link was simulated using a printed circuit board in which a power transfer efficiency (PTE) of 2.11% was achieved at a distance of 3 cm using a transducer of dimensions 1 mm³ operating at 1.8 MHz .

Galluccio et al. [31] successfully demonstrated a proof-of-concept for a hybrid bi-directional implant of mm-scale dimensions placed in chicken meat with an acoustic intensity of 0.36 mW/mm², which is 5% of the FDA limits. The implant was powered using ultrasound and RF (UWB pulses) to communicate with an external receiver and could support a direct current (DC) load power of 100 μ W with dimensions of 4 mm x 7.8 mm. A study on wireless power transfer using ultrasound operating at 1 MHz frequency was demonstrated in the work of Mazzilli et al. [44], where a PTE of 2.3% was achieved in water without the use of any phantom material and a drop of 1.6% using phantom material at a distance of 105 mm.

Tsai et al. [45] demonstrated a wireless neural stimulation device powered by ultrasound that achieved a bit error rate (BER) of 10^{-6} at a data rate of 25 kbps, which was tested using frequency-shift keying (FSK), phase-shift keying (PSK), and ASK. Here they used a piezoelectric polyvinylidene fluoride (PVDF) transducer 6 mm in diameter operating at 1 MHz

frequency and were able to receive a power ranging from 4.15mW to 19.76 mW by regulating the transmit power without exceeding the FDA limits. A theoretical study over ultrasound powering showed an acoustic intensity greater than 0.1 W/cm^2 can be achieved by limiting the acoustic radiated power that is within FDA limits and thermal effects of the implant and for distances between 100–150 mm [46].

An implantable device that can be remotely actuated by ultrasound for measuring various tissue parameters such as pH, temperature, electrolyte concentration, and biopotentials was also demonstrated [47]. The device operates at 0.8 V with a total current consumption of 60 μA when excited by an sinusoid ultrasound source operating at a frequency of 400 kHz and a power density of 20 mWcm^{-2} . An implantable micro-oxygen generator for in situ tumor oxygenation was studied and implemented in-vivo and in-vitro. The overall dimensions of the device were $1.2 \text{ mm} \times 1.3 \text{ mm} \times 8 \text{ mm}$ and could generate a current of 150 μA when powered using ultrasound operating at a 2.15 MHz frequency using a piezoelectric transducer (PZT).

One study and implementation that very closely shares the goals of the work in this thesis was presented by Seo et al. [36], but this work is specific to brain-machine interfaces (BMIs). The model presented in this work uses a low power CMOS circuitry, which implements ultrasound for power delivery and backscatter communication. An ultra-miniature device to detect and report local extracellular electrophysiological data of dimensions 10 μm and 100 μm using 65 nm technology were analyzed and proposed. An interrogator placed in the sub-cranial region of the brain helps in establishing a power and communication between the implant and external device. For a device of dimensions 100 μm placed at a depth of 2 mm in the brain and a signal-to-noise ratio (SNR) of 3, it has been shown to achieve a PTE of 7% (-11.6 db), resulting in total receiver power 500 μW using an interrogator of dimensions 1 mm^2 . With further

improvement in efficiencies in the ultrasound link, the device could further scale down to 10's of μm . Here, BaTiO_3 was used as the PZT.

Ozeri and Shmilovitz [48] demonstrated ultrasonic transcutaneous energy transfer (UTET) for data and power transfer. This study, experimentally done in a water tank with a distance of 150 mm between the source and the implant, was able to achieve a data rate 1200 bits/s using ASK with 9% load resistance variation known as impedance modulation and simultaneous transfer of 20 mW of power. The feasibility of using ultrasound for intrabody communication is been studied by Galluccio et al. [49] and various attributes related to communication, such as ultrasound propagation in tissue, transmission frequency, power, bandwidth, size, and the challenges to implement a network of devices operating on ultrasound were thoroughly discussed and analyzed.

Acoustic Transducers: Acoustic waves are converted to AC voltage using acoustic transducers. There are two types of transducers that are generally used: capacitive ultrasonic transducer (CUT) and piezoelectric transducer (PZT). With the CUT, the incident acoustic wave is converted to electrical voltage through the capacitance change. Since the operating voltages of the CUT are high, they are not suitable as transducers in IMD [13, 50, 51]. With the PZT, piezoelectric materials and fabrication methods have shown rapid development due to their increased application, which has led to the manufacturing of miniaturized transducers at microscale and nanoscale [52, 53, 54, 55, 56, 57], thus making them more suitable for IMD-based applications.

In the PZT, the incident acoustic wave is converted to electrical voltage through the piezoelectric effect. Piezoelectricity refers to the ability of converting mechanical motion to electricity, and vice versa. Therefore, the state change is possible by either mechanical

deformation or by electrical stimulation. The materials that exhibit such a phenomenon play a vital role in building small-scale implants powered through ultrasound. Since ultrasound is used in imaging in the field of medicine, a myriad of transducers that are application specific are available in the market such as PVDF, PZT, LiNbO₃, AlN, ZnO, BaTiO₃, PVDF . The popular piezoelectric single crystals used for ultrasonic transducer applications are PMN-PT and PIN-PMN-PT [58]. Since piezoelectric ceramics have relatively high coupling capability and low dielectric loss, they have been widely used in electromechanical applications [1]. Among the ceramics, Pb (Zr, Ti)O₃ (PZT) ceramics are widely used. PVDF, LiNbO₃ are advantageous for large aperture single-element-based applications due to their low dielectric permittivity. PZT is known for its high performance, sensitivity, electromechanical coupling coefficient, therefore it is used in diagnostic ultrasound imaging [59]. The lead content of PZTs makes them harmful to use in humans. This has led to the introduction of biocompatible material that is similar to PZT, such as AlN, BaTiO₃ and ZnO [60].

2.1.4 Radio Frequency

Radio frequency ranges from 30 kHz to 300 GHz (3THz), as shown in Figure 3.

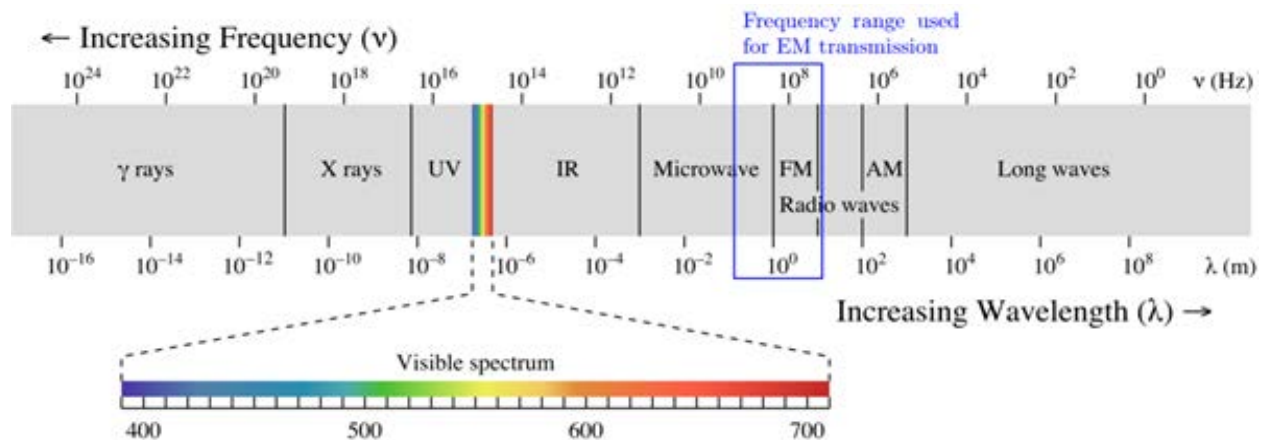


Figure 3. Electromagnetic spectrum [61].

RF can be used as a source for both powering and communication. According to the energy transmission mechanism, the existing wireless energy transmission techniques can mainly be classified into the following three types [62]:

- Electromagnetic radiation wireless energy transfer (far-field).
- Non-radiated inductively coupled energy transfer (ICPT) (near-field).
- Non-radiation magnetic resonance wireless energy transfer (near-field).

One of the most widely acknowledged solutions for wireless power transfer (WPT) to power the IMD is magnetic or inductive coupling (near-field, non-radiative) at radio frequency [64, 65, 66]. Radiative modes of omnidirectional antennas (which work very well for information transfer) are not suitable for such energy transfer because a vast majority of energy is lost into free space. Both near-field and far-field regions of a coil are shown in Figure 4.

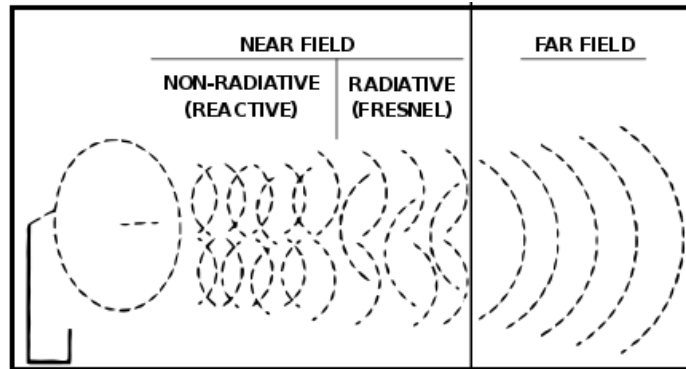


Figure 4. Near-field and far-field radiation of a coil [63].

The concept of mutual induction known as near-field communication (NFC) is the primary concept used in wireless powering of mobile phones, radio frequency identification (RFID), mobile pay (Samsung pay), etc. Magnetic induction is based on Faraday's law, which states that a time-varying magnetic field through a surface bounded by a closed path induces a voltage around the loop. The principle behind this is based on a mutual inductance between two coils in which one is located outside the body while the other is integrated with the implanted

device. As the external coil transmits a varying electromagnetic signal, a voltage would be induced in the receiver coil (IMD). Two electromagnetic systems are weakly coupled for a certain distance of separation. However, if the two systems have the same natural resonant frequency, they can excite strong magnetic resonance (non-radiation magnetic resonance wireless energy transfer).

The biggest advantage and reason why RF(near-field) is widely used as a source of powering is because it uses a magnetic field that does not interfere with biological tissue. The magnetic permeability of various biological tissues is shown in Table 1. Permeability is the measure of the ability of a material to support the formation of a magnetic field within itself.

TABLE 1

ELECTROMAGNETIC FIELD PROPERTIES IN DIFFERENT HUMAN TISSUES. [69]

Tissue	μ	σ (S/m)	ϵ ($\mu\text{F/m}$)
Brain White Matter	1	0.142	1
Brain Gray Matter	1	0.33	1
Cerebrospinal Fluid	1	1.53	1
Bone	1	0.0054	1
Muscle	1	0.11	1
Fat	1	0.04	1
Soft Tissue	1	0.173	1
Skin	1	0.435	1

Various models have been proposed and used for the effective transfer of power using magnetic induction. A RF tag was fabricated using a 0.18- μm CMOS with dimensions of 0.68 mm^2 and a power consumption of 67.7 μW given a power supply of 1.8 V [67]. Inductive coupling was improvised to power extremely small devices using mid-field powering to create a high-energy density region in the tissue. The implant using this method could transfer power of

a few milliwatt's to a micro implant of dimension 2 mm placed at a distance > 5 cm inside the chest with exposure levels below safety thresholds for humans [68].

In the work of Jow and Ghovanloo [70], the power transfer efficiency in tissue was optimized using printed spiral coils (PSCs). These coils were used to optimize a wireless link of a 1 cm^2 implantable device, and they achieved a PTE of 30.8% at a distance of 10 mm in muscle. Another example of using inductive coupling to power is for demonstrated using a wireless camera capsule for non-invasive visual inspection of the small bowel operating at a frequency of 1 MHz [71]. This power source could generate up to 150 mW using a coil of dimensions $10 \times 13 \text{ mm}^2$ at a distance of 205 mm from the source. Using PSCs operating at 13.56 MHz, a PTE of 58% is achieved at an implantable coil of dimensions of 25 mm x 10 mm x 0.5 mm in the tissue environment at a distance of 10 mm [72].

A variant of inductive coupling involving a four-coil system rather than a two-coil system of inductive coupling was proposed [73]. It was shown to have twice the efficiency of inductive link models using two coils of the same size and operating range. A PTE of 82% and 72% was achieved at 20 mm and 32 mm, respectively, for an implant coil with a diameter of 22 mm. The small change in the PTE with respect to the distance shows the robustness of the system for long-range powering. Another variant of inductive coupling which happens in the near-field is mid-field wireless powering, which is implemented in the low gigahertz range in contrast to frequencies of (< 10 MHz) of inductive coupling [74, 75]. When the implant is much smaller than its distance from the source, which is usually the case in an implant, the coupling between the coils becomes weak. Inductively coupled coils operating in this weakly coupled regime are usually very inefficient. In such cases, high efficiencies can be obtained using mid-

field powering, where the power transfer occurs through a combination of inductive and radiative modes.

2.1.5 Terahertz

Terahertz (THz) radio frequency can be used for communication only, not for powering an implantable medical device. Since these devices are at micro-nanoscale, they require an antenna of the same scale, which leads to an increase in the operating frequency to terahertz. In the last few years, many have studied the possibility of using THz for communication. Terahertz is used in the THz band between 0.1 and 10 Thz. Many challenges must be overcome in order to implement them. A line of sight (LOS) is needed in order to communicate, and there is a very high path loss due to the high operating frequency. Using THz in the human body becomes even more difficult since it is very difficult to attain an LOS such a complex environment [76]. With these present challenges, it is not possible to implement communication using Thz inside the human body.

2.2 Communication

2.2.1 Modulation

Modulation is a process of representing the information/message to be transmitted by changing different characteristics of the signal, such as frequency, amplitude, and phase. Apart from representing data, modulation also offers resilience to channel impairments, depending upon the type of modulation. ASK, FSK, and PSK are the modulation techniques that are most widely used in implants. Given a certain bandwidth, modulation contributes directly to the data rate. A data rate of approximately 10% of the carrier frequency is achievable using the basic modulation schemes (ASK, PSK, FSK). More complex modulations to achieve higher data rates can be attained by combining multiple modulation schemes or varying the basic

modulation techniques, such as delta, on-off keying (OOK), distributed frequency-shift keying (DFSK), and quasi-coherent phase-shift keying (QCP SK). The choice of modulation methodology depends upon the following:

- High data rate.
- High spectral efficiency (minimum bandwidth occupancy).
- High power efficiency (minimum required transmit power).
- Robustness to channel impairments (minimum probability of bit error).
- Hardware implementation complexity—low power/cost implementation.

Since most of these factors are equally important under normal conditions, a tradeoff between them determines the choice of the modulation scheme. In this thesis, since the main limitation is size, the choice of modulation depends upon the complexity because it dictates both size and power required to implement.

Modulation involves two signals: one is the message/data signal $\mathbf{m}(\mathbf{t})$, and the other is the carrier signal $\mathbf{c}(\mathbf{t})$. Since frequency of the signal transmitted has an inverse relationship with the size of the antenna, a high frequency signal $\mathbf{c}(\mathbf{t})$ is typically used to restrict the size of the antenna. Also, since the message signal is digital, it is represented as either 0's or 1's.

2.2.2 Performance Measure

Space and power are scarce resources in an IMD; therefore, performance of every component must be evaluated with respect to these two parameters. For example, if a modulation scheme has a data rate of L kbps, then the value of L alone cannot capture the performance of this modulation scheme. Rather, the die area and the power required by its circuitry must also be taken into consideration. Therefore, a new measure of performance is

needed when different methods for designing each building block are investigated. The following ratio is typically used for this purpose:

$$\text{Performance measure} = \frac{\text{stand – alone performance}}{\text{diearea}(\mu\text{m}^2) \times \text{power}(\mu\text{W})} \quad (1)$$

Table 2 lists state-of-the-art in low power, low area modulation in terms of the performance measure

TABLE 2
STATE-OF-THE-ART IN LOW-POWER, LOW-AREA MODULATION IN TERMS OF PERFORMANCE MEASURE

Reference	Modulation	Area (mm ²)	Power Consumed (μW)	Data Rate (kbps)	Performance Measure $\frac{Kbps}{\mu m^2 \times \mu W}$	CMOS Technology	Implemented/Simulated
[77]	ASK		0.0453	40-160		90 nm	Simulated
[78]	ASK		0.95	6000		65 nm	Implemented
[79]	Delta		0.3			65 nm	Simulated
[80]	ASK	3.2	0.58	1000	0.0005	0.35 μm	Simulated
[81]	ASK		0.062	1		0.35 μm	Simulated
[82]	OOK	0.3	23–69	4000	0.0005	0.13 μm	Implemented
[83]	FSK	0.003	22	450	0.0075	0.35 μm	Simulated
[84]	QCPSK	0.005	59	800	0.0027	0.18 μm	Implemented
[85]	PSK	1.5x1.6		32	4.2x10 ⁻⁷	0.35 μm	Implemented

CHAPTER 3

PROPOSED SYSTEM AND RELATED PARAMETERS

3.1 Proposed System

Performance of both powering and communication are analyzed on the basis of the efficiency of wireless transfer of power. In wireless communication, the performance is calculated using the BER, which in return depends upon the signal strength received at the receiver. Chapter 2 reviewed the various ways of transferring power to the IMD, each of which has its own pros and cons. When it comes to energy-harvesting techniques, the present state-of-the-art does not have the capability of efficiently converting the available power, and the source of energy restricts the implant location. Terahertz communication undergoes a large attenuation in tissues, thus restricting the communication range to mm, since it requires a LOS to communicate that is difficult to achieve in an environment like human body. In spite of RF being a very mature field, using RF in lower frequencies by inductive coupling is not an effective way to power the implant, due to the fact that in order to induce high voltages, the dimensions of the required coil would exceed the size limitation of the implant. RF using higher frequencies where radiation of the antenna is used is highly ineffective because of its higher attenuation due to operating at higher frequencies. By adhering to FDA limitations on RF, it is difficult to achieve good PTE.

Ultrasound is ineffective for communication because in order to communicate with an external device, it has to pass through the air-tissue interface in which about 99.9 % energy is lost (which will be explained in section 3.3.3). Also, the limited amount of power available at the implant makes it even worse, whereas it could be used for external powering for the following reasons: one, it has excellent propagating properties in a medium composed of water;

two, with external powering, there is no size limitation and more freedom on power; and three, even with the FDA limited intensity, it is good enough to induce an adequate amount of voltage (will be shown in this chapter). Optical devices are good for neither communication nor powering since large attenuation occurs in a tissue environment and requires the concentration of power at some point, which in the case involving multiple sensors is not possible.

In models which use the same form of energy (optical, ultrasound, RF), it is not possible to effectively achieve both powering and communication because of their disadvantages, as explained previously. Therefore, for the research in this thesis, a hybrid model, referred to as a bio-mote, is used, as shown in Figure 5. The bio-mote uses two different forms of energy for powering and communication, depending upon their advantages. The literature indicates that ultrasound and inductive coupling are the most analyzed and used techniques. Using ultrasound is the best way to achieve power with less loss, compared to inductive coupling especially over long distances [29]. Ultrasound could be effective when used externally rather than in an implant because there is access to an adequate amount of power, which is not the case with an implant. In order to overcome the air-tissue problem, inductive coupling is used for communication. Even though Inductive coupling is not as effective as ultrasound, since external devices (mobile phone), as shown Figure 6, have an abundant access to processing capabilities, and a good data rate can be achieved.

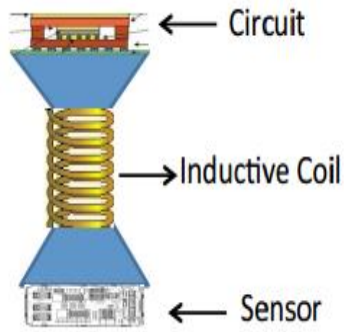


Figure 5. Bio-mote with inductive coil and bio sensor

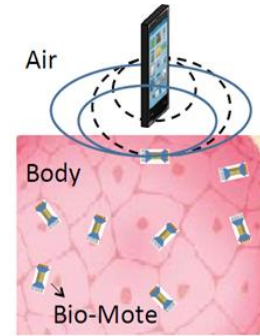


Figure 6. Cell phone (reader) powering communicating with motes in its read zone

This chapter explains in detail the parameters used to implement inductive and ultrasound models in order to analyze the performance of the hybrid bio-mote device, as shown in Figure 7.

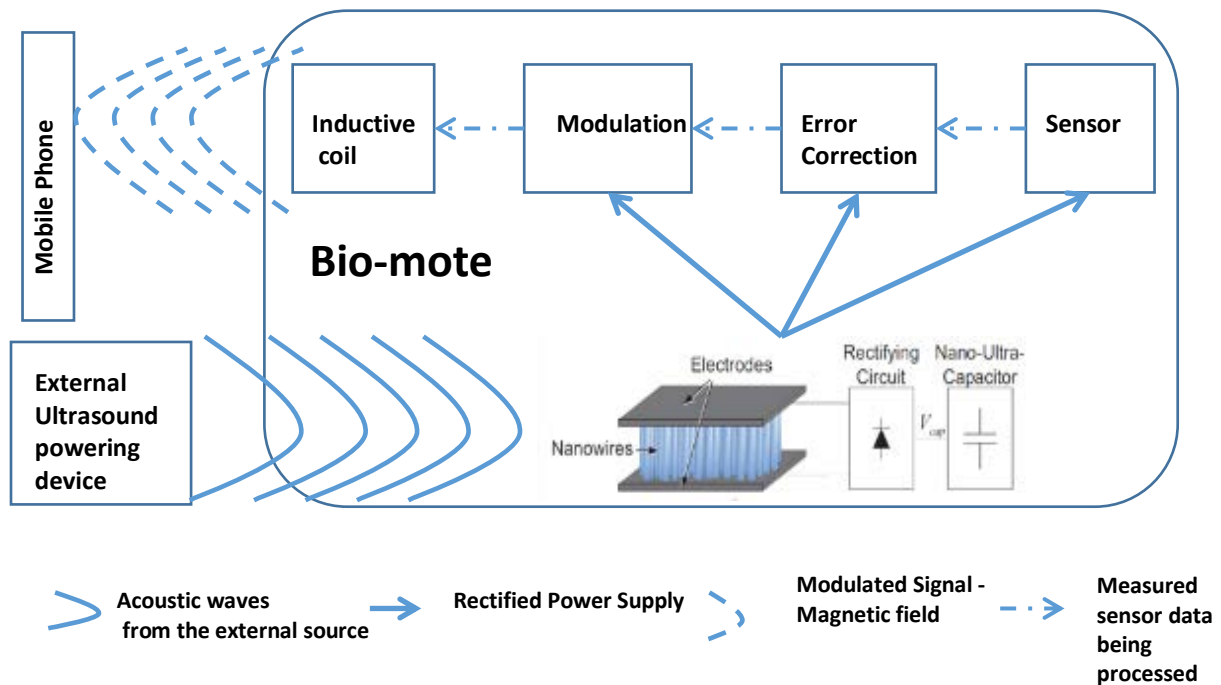


Figure 7. Complete block diagram of process involved in proposed bio-mote system.

3.2 Inductive Coupling Parameters

The wireless power transfer (WPT) efficiency depends on the resonance frequency (or operating frequency), distance, alignment, and coupling matching between the transmitter and

the receiver coils. WPT uses inductive coupling by utilizing a magnetic field. According to Ampere's law, the current flowing in a conductor produces a magnetic field around the conductor. The magnetic field produced by a current element on a round conductor (wire) with a finite length is given by [86]

$$B_{\phi} = \frac{\mu_0 I}{4\pi r} (\cos \alpha_2 - \cos \alpha_1) \text{ (Weber/ m}^2\text{)} \quad (2)$$

The magnetic field produced by a circular loop antenna is given by

$$\begin{aligned} B_z &= \frac{\mu_0 I N a^2}{2(a^2 + r^2)^{3/2}} \\ &= \frac{\mu_0 I N a^2}{2} \left(\frac{1}{r^3} \right) \quad \text{for } r^2 \gg a^2 \end{aligned} \quad (3)$$

where

I = current

a = radius of loop

r = distance from center of loop

μ_0 = permeability of free space and given as $4 \pi \times 10^{-7}$ (Henry/meter)

3.2.1 Mutual Induction

Mutual inductance is a function of coil geometry and the spacing between coils. Mutual inductance occurs between the external coil and the implant, and is given by

$$M = \left[\frac{\mu_0 \pi N_1 N_2 (ab)^2}{2(a^2 + r^2)^{\frac{3}{2}}} \right] \quad (4)$$

where

V = voltage induced in the implant coil

i_1 = current on the external coil

a = radius of external coil

b = radius of implant coil

r = distance between two coils

3.2.2 Induced Voltage

A generalized expression for the induced is given by equation (5) [86]

$$V_0 = 2\pi f N S Q B_0 \cos\alpha \quad (5)$$

where

f = frequency of arrival signal

N = number of turns of coil in loop

S = area of loop in square meters (m^2)

Q = quality factor of circuit

B_0 = strength of arrival signal

α = angle of arrival of signal

From equation (5), it can be said that the voltage induced in the implant coil depends upon the quality factor (Q), frequency, magnetic field strength, and area of the coil.

3.2.3 Direct Current Resistance

The direct current resistance for a conductor with a uniform cross-sectional area is given by [86]

$$R_{DC} = \frac{l}{\sigma S} = \frac{l}{\sigma \pi a^2} \quad (\Omega) \quad (6)$$

where

l = total length of wire

σ = conductivity of wire (mho/m)

S = cross-sectional area or πr^2

a = radius of wire

3.2.4 Alternating Current Resistance

Resistance of the wire changes depending upon either an alternating current (AC) or DC current flowing through the wire. Since inductive coupling requires a varying magnetic field, this involves AC resistance of the wire rather than DC resistance.

3.2.5 Skin Effect

Dealing with AC leads to phenomenon called skin effect, where the resistance of the wire varies with the frequency of the AC current flowing through it, rather than the resistance being constant, as in the case of DC. An alternating current in a conductor produces an alternating magnetic field in and around the conductor. In turn, the change in the magnetic field creates an electric field that opposes the change in current intensity. This opposing electric field is strong at the center of the conductor and forces the conducting electrons to the outside of the conductor. As a result, the current density decreases in the center of the wire and increases near the edge of the wire. This effect is referred to as the skin effect. The net result of the skin effect is an effective decrease in the cross-sectional area of the conductor and, therefore, a net increase in the AC resistance of the wire. The skin depth and AC resistance are given as

$$\delta = \frac{1}{\sqrt{\pi f \mu \sigma}}$$
$$R_{ac} = \frac{l}{\sigma A_{active}} \approx \frac{l}{2\pi a \delta \sigma} \quad (7)$$

where the skin depth area on the conductor is $A_{active} \approx 2\pi a\delta$.

3.2.6 Parasitic Capacitance

An ideal inductor has only an inductance value but no resistance or capacitance. However, real inductors are comprised of other parameters such as resistance (due to resistance of the wire and skin effect) and parasitic capacitance (due to the electric field between the wire turns, which are at slightly different potentials) and can be modeled as shown in Figure 8 [87]. These parameters become more pronounced at higher frequencies, and there lies a frequency point where real inductors behave as resonant circuits, thereby becoming self-resonant.

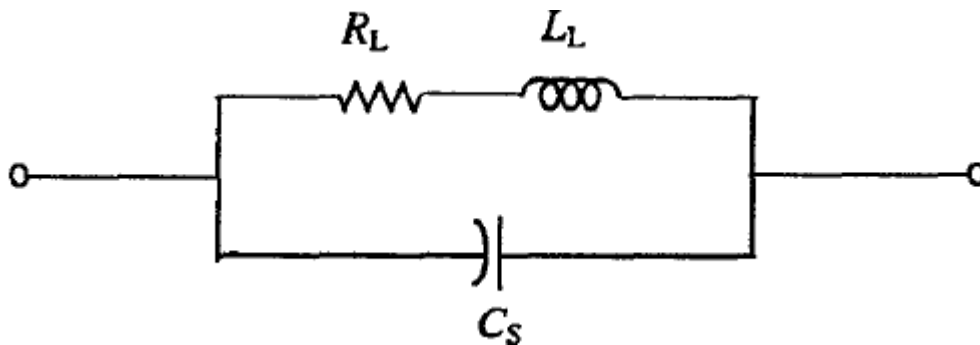


Figure 8. Inductance circuit model in terms of resistor, inductor, and capacitor (RLC) [88].

3.3 Ultrasound Parameters

An ultrasound transducer as explained in 2.1.3 resonates at its natural frequency once excited by an electrical source and vice versa. In any power transfer application, the impedance matching between the device and the surrounding area plays an important role. In the case of a piezoelectric device placed inside the human body as an implant, the material itself has much higher acoustic impedance when compared to that of approximately biological tissue or water. This mismatch of impedance causes a very large loss of acoustic energy. The impedance mismatch is usually resolved using a matching layer on the transducer by mixing micro- or

nanoscale powder, whereby the impedance of the matching layer (powder) can be varied by varying the size of the powder. Another approach for matching the layers is with a coating of polymer on the transducer [58, 89, 90, 91]. An ultrasonic transducer can be modeled using one-dimensional circuit models. The most popular adopted by many is the KLM model [92].

3.3.1 Size and Frequency Trade-Off

Size determines the resonating frequency of the transducer. It is inversely proportional to the ratio of the diameter of the radiating surface and the wavelength, and can be related using equation 8 [27, 5]:

$$f_r = \frac{c}{2t} \quad (8)$$

Since an IMD requires small-scale implementation, the transducer must operate at higher frequencies due to the inverse relationship. According to the absorption loss equation, the absorption of ultrasound at high frequency is high, leading to high attenuation values, as explained next in section 3.3.2. Therefore, a trade-off should exist between size, frequency, and attenuation. In order to satisfy the IMD limitations and specifications, the transducer must operate at the lowest possible frequencies that are compatible with the IMD's size limitation.

3.3.2 Attenuation

As sound propagates in any medium, its intensity (pressure output power per unit area) decreases. This is known as attenuation, depending upon the properties of the medium and the sound. Attenuation depends on two factors

- Absorption Loss – Varies with frequencies
- Spreading Loss – Varies with distance from the transducer

Relative to absorption loss, as ultrasound propagates inside the body, the energy is absorbed by the surrounding medium, in the case here, human tissue. This is due to the absorption of the acoustic energy by the tissue, whereby heat is generated. A part of the incident acoustic energy is converted to heat by the tissue, thereby playing a role in the attenuation. Heat dissipation is a very important factor in the IMD since it must follow FDA regulations.

The dispersion of the acoustic wave in the medium leads to spreading loss. In a homogenous and infinitely extended medium, since the total area of the pressure wave surface increases with distance, the energy is spread for that area. The energy spread with an increase in distance leads to a decrease in the acoustic intensity of sound.

Attenuation in human tissue varies with the tissue acoustic properties and the frequency of the constant wave, as can be seen in Figure 9.

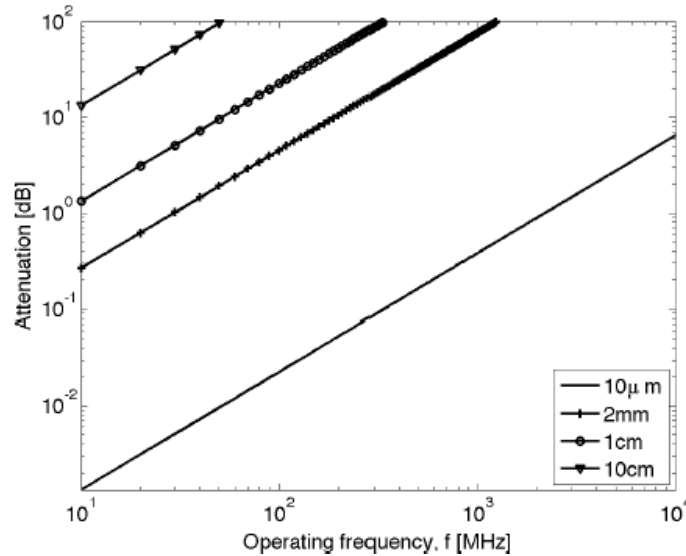


Figure 9. Attenuation over various distances and operating frequencies [30].

It has been shown [93, 94, 95, 96, 97, 27] that attenuation can be modeled in terms of frequency and distance as

$$P(d) = P_0 e^{-\alpha d} \quad (9)$$

where α is the absorption coefficient, which is a function of frequency and is given by

$$\alpha = a f^b \quad (10)$$

where α is (in [np. cm⁻¹]). The amplitude attenuation coefficient \mathbf{a} (in [np m⁻¹ MHz^{-b}]) is solely dependent on the material and is measured in dB/cm/MHz. The values of a and b have been calculated and presented in many papers, and have been shown to vary for different parts of the body [95, 98, 99]. The value of b is considered 1 for soft tissues [96]. Table 3 is a list of attenuation coefficients and velocity of acoustic waves in various tissues [70].

TABLE 3

LIST OF ATTENUATION COEFFICIENTS AND VELOCITY OF ACOUSTIC WAVES IN VARIOUS TISSUES [70]

Tissue	Density ρ (kg m ⁻³)	Velocity of sound c (m s ⁻¹)	Attenuation coefficient $\alpha = af^b$			Nonlinearity parameter B/A
			α (10 ² neper m ⁻¹)	a (10 ² neper m ⁻¹ MHz ^{-b})	b	
Amniotic fluid	965	1534	0.0093 @ 5 MHz	—	—	—
Blood	1055	1584	0.095–0.13 @ 5 MHz	0.014–0.018	1.19–1.23	6.0
Bone (skull)	1610	2190–3289	9.0 @ 3 MHz	—	—	—
Bone (trabecular)	1920	1688–2407	0.22–1.8 @ 0.2–1.0 MHz	—	—	—
Brain	1030–1041	1562	0.46–0.72 @ 5 MHz	0.067–0.069	1.20–1.46	6.5–7.6
Breast	1020	1430–1570	0.96 @ 5 MHz	0.086	1.5	—
Eye (lens)	1034–1113	1640–1673	0.9 @ 10MHz	—	—	—
Eye (vitreous humor)	1009	1523–1532	0.07 @ 6 MHz	—	—	—
Fat	917–939	1412–1487	0.56 @ 6 MHz	—	—	9.6–10.3
Heart	1044 ⁺	1571 ⁺	0.23 @ 1 MHz	—	—	6.8
Kidney	1050	1560–1580	0.23 @ 2 MHz	—	—	5.8–9.0
Liver	1050–1070	1578–1640	0.17–0.57 @ 5 MHz	0.041–0.070	0.9–1.30	5.5–7.6
Muscle (skeletal)	1038–1056	1529–1629	0.54 @ 4.3 MHz	—	—	7.4–8.1
Pancreas	1040–1050	1591	0.42 @ 5 MHz	0.12	0.78	—
Skin (epidermis)	1110–1190	1729 ⁺	1.06 @ 5 MHz	—	—	7.9
Spleen	1054	1567–1635	0.23–0.66 @ 5 MHz	0.036–0.062	1.14–1.47	7.8
Teeth (dentine)	2030–2350	3140–4140	9.2 @ 18 MHz	—	—	—
Teeth (enamel)	2890–3020	4500–6250	14.0 @ 18 MHz	—	—	—
Testes	1044	1595	0.3 @ 5 MHz	0.02	1.7	—

3.3.3 Reflection

It is possible to predict the way that ultrasound propagates and interacts with tissue by knowing the wave properties, such as velocity, absorption, attenuation, and reflection. As sound

travels from one medium to another, it undergoes reflection, wherein only part of the wave is allowed to travel into a medium. The fraction of the impinging energy reflected from an interface depends on the difference in acoustic impedance of the media on opposite sides of the interface.

The acoustic impedance Z of a medium is the product of the density ρ of the medium and the velocity of ultrasound in the medium:

$$Z = \rho c \quad (11)$$

The acoustic impedances of several materials are listed in Table 4.

TABLE 4
ACOUSTIC IMPEDANCE OF DIFFERENT BODY TISSUES [69].

Body Tissue	Impedance (kg/m ² -sec)	Body Tissue	Impedance (kg/m ² -sec)
Air	400	Liver (25°C)	1.65 x 10 ⁶
Lung	1.80 x 10 ⁵	Blood	1.65 x 10 ⁶
Fat	1.39 x 10 ⁶	Nerve (optic)	1.68 x 10 ⁶
Aqueous humor	1.51 x 10 ⁶	Muscle	1.73 x 10 ⁶
Water	1.52 x 10 ⁶	Lens of eye	1.84 x 10 ⁶
Brain (25°C)	1.57 x 10 ⁶	Nylon	2.9 x 10 ⁶
Skin	1.6 x 10 ⁶	Skull bone	7.80 x 10 ⁶
Soft tissue (avg.)	1.63 x 10 ⁶	Enamel	1.71 x 10 ⁷
Kidney	1.63 x 10 ⁶	Diamond	6.3 x 10 ⁷

For an ultrasound, the acoustic impedance may be expressed in units of rayls, where a rayl = 1 kg-m⁻²-sec⁻¹. At each tissue interface, the energy carried by the wave will suffer reflection. Sound in any medium travels in a straight line. When the wave front reaches an interface between media that has different characteristic impedances, then the wave undergoes reflection and refraction. Snell's law applies to this case; therefore, the reflectivity R of the wave, which describes the percentage of the incident wave that is reflected, can be calculated by [40]

$$R = \frac{p_r}{p_i} = \frac{Z_2 \cos \theta_i - Z_1 \cos \theta_t}{Z_2 \cos \theta_i + Z_1 \cos \theta_t} \quad (12)$$

With a large impedance mismatch at an interface, much of the energy of an ultrasound wave is reflected, and only a small amount is transmitted across the interface, which is the case for an air-tissue interface. As shown in Table 5, it is calculated that 99% of the acoustic energy would be reflected back for an air-tissue interface [69].

TABLE 5
AMOUNT OF ENERGY REFLECTED BACK WHEN ULTRASOUND PASSES THROUGH
VARIOUS INETRFACES [69]

Tissue Interface	Energy Reflected	Energy Transmitted
Kidney/Liver	0.0036%	99.9964%
Liver/Muscle	0.032%	99.968%
Muscle/Blood	0.07%	99.93%
Soft tissue/Water	0.23%	99.77%
Fat/Kidney	0.64%	99.36%
Lens/Vitreous humor	0.91%	99.09%
Fat/Liver	1.00%	99.00%
Lens/Aqueous humor	1.04%	98.96%
Fat/Muscle	1.08%	98.92%
Bone/Muscle	41.23%	58.77%
Soft tissue/Bone	43.50%	56.50%
Bone/Fat	48.91%	51.09%
Soft tissue/Lung	63.64%	36.36%
Diamond/Water	90.80%	9.20%
Muscle/Air	98.01%	1.99%
Water/Air	99.89%	0.11%
Soft tissue/Air	99.90%	0.10%
Diamond/Air	99.997%	0.0025%

3.4 Modulation and Related Parameters

As explained in 2.2.1 we only consider ASK and BPSK modulation due to their simplicity. The performance of modulation is often measured using the parameter BER. BER is defined as the ratio of number of bits in which error has occurred and the total number of bits transmitted:

$$\text{BER} = \text{Number of Error Bits} / \text{Total Number of Bits}$$

The average energy per bit (E_b) for a signal $x_m(t)$ E_b is expressed as

$$E_b = \int_0^{T_b} x_m^2(t) dt \quad (13)$$

The Q function is defined as the probability that a Gaussian random variable x with mean zero and variance one is bigger than z :

$$Q(x) = p(x > z) = \int_z^{\infty} \frac{1}{\sqrt{2\pi}} e^{-\frac{y^2}{2}} dy \quad (14)$$

3.4.1 ASK

Amplitude-shift keying is one of the most adopted modulation techniques in bio implants. With ASK, the amplitude of the carrier is varied with respect to the message signal, as shown in Figure 10.

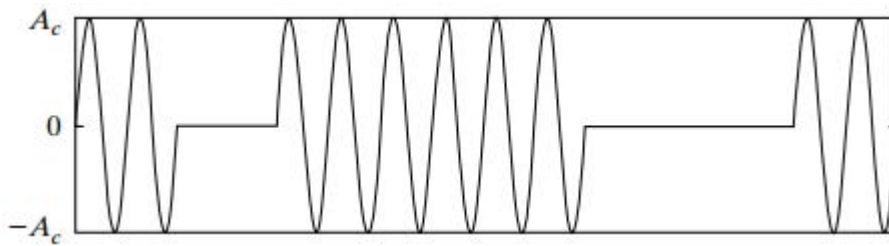


Figure 10. Amplitude shift keying.

The modulated message signal $x(t)$ can be represented as

$$\begin{aligned} x(t) &= A_c \cos(2\pi f_c t) && \text{symbol "1"} \\ x(t) &= 0 && \text{symbol "0"} \end{aligned}$$

where each symbol (0,1) is defined in terms of the carrier $\cos(2\pi f_c t)$, and f_c is the carrier frequency. Both bits 0 and 1 are represented in terms of amplitude, and in order to detect the ASK-modulated signal at the receiver and to reduce the number of errors, there should be a good amount of difference between the amplitudes that represent 0,1. This difference is measured by a term

referred to as modulation index (depth). For ASK,

$$m \% = \left(\frac{A_1 - A_0}{A_1} \right) \times 100\% \quad (15)$$

ASK is usually vulnerable to noise; therefore, modulation is often chosen to be high. Modulation depth could even be 100%, in which case it is referred to as OOK modulation. Using this scheme could be power efficient since no signal is transmitted for the bit 0. The BER for ASK is

$$P_b = Q \left(\sqrt{\frac{E_b}{2N_0}} \right) \quad (16)$$

3.4.2 BPSK

In binary phase-shift keying, the phase of the signal is varied depending upon the information bits, as shown in Figure 11, where the two bits are represented with a 180° phase shift.

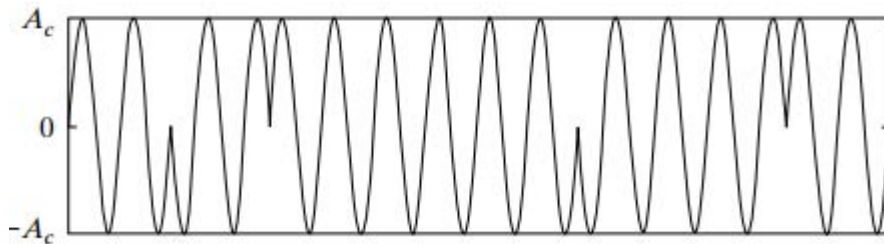


Figure 11: Binary phase-shift keying.

The phase change of 180° can be represented as

$$\begin{aligned} x(t) &= A_c \cos(2\pi f_c t) && \text{symbol "0"} \\ x(t) &= A_c \cos(2\pi f_c t + \pi) = -A_c \cos(2\pi f_c t) && \text{symbol "1"} \end{aligned}$$

The BER for BPSK [100] is

$$P_b = Q\left(\sqrt{\frac{2E_b}{N_0}}\right) \quad (17)$$

3.5 Error-Correction Coding and Related Parameters

The number of errors determines the efficiency of a communication system. According to Shannon, an arbitrarily low error probability could be obtained using coding on any channel, provided that the bit-rate is below the capacity of the channel. Modulation helps in controlling the number of errors occurring as a result of the channel only to a certain extent, but using error-correction techniques could further reduce the number of errors. The general idea of error control codes is to let the transmitter include a few additional bits to the information to be transmitted in a clever way so that the receiver can detect or correct the most probable error patterns introduced by the channel.

Different error control mechanisms have been adopted over years and are categorized as follows:

- Linear Block Codes
- Convolution
- Hybrid

Codes that implement complex logic tend to achieve a lower bit error rate, but they are difficult to implement on small-scale devices. To the best of our knowledge, short linear block codes which are Hamming codes and Reed-Solomon codes are the best choice for implementing error control in the bio-mote since they are less complex and could be implemented at micro-scale. So we focus on Hamming and RS codes.

In the work here, the bio-mote can only send information therefore we are concerned only with the encoding rather than decoding. This is quite advantageous because in most error-correction mechanisms, decoding is much complex process than encoding.

3.5.1 Reed-Solomon Codes

Reed-Solomon (n, k) codes with m-bit symbols exist for all n and k for which $0 < k < n < 2^m + 2$, where k is the number of data symbols being encoded, and n is the total number of code symbols in the encoded block [112]. While encoding the information, which is the form of symbols (a combination of bits), it can be mapped to an element in the field called Galois field. This mapping is using done with the help of a generator polynomial. If an (n, k) code is cyclic, then it can be shown that the code can always be defined using a generator polynomial. A generator polynomial is a primitive polynomial, and a primitive polynomial for every degree has already been calculated and documented as

$$g(x) = g_0 + g_1x + g_2x^2 + \dots + g_{n-k}x^{n-k}$$

Reed-Solomon codes are non-binary cyclic codes with symbols made up of m-bit sequences, where m is any positive integer having a value greater than 2. The generator polynomial construction for Reed-Solomon codes is the approach most commonly used today in the error control literature.

For RS codes, a vector c is a code word in the code defined by g(x), if and only if its corresponding code polynomial c(x) is a multiple of g(x), as shown in equation (18). This provides a very convenient means for mapping information symbols onto code words.

$$c(x) = m(x) \times g(x). \tag{18}$$

Relative to hardware implementation, RS codes have been implemented using flip flops formed of XOR gates used in memory devices [102, 103]. They can also be implemented using

shift registers, as shown in Figure 12, which is an implementation of RS (7,3) encoding.

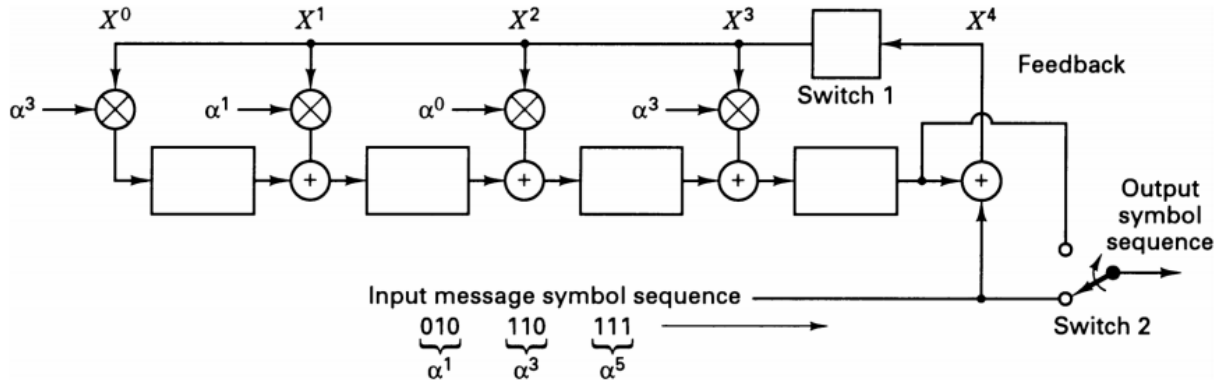


Figure 12. Implementation of RS (7,3) using shift registers [101].

Relative to error-correction capability: For the most conventional R-S (n, k) code, $(n, k) = (2^m - 1, 2^m - 1 - 2t)$, where t is the symbol-error correcting capability of the code, and $n - k = 2t$ is the number of parity symbols. For RS codes, the minimum distance between codeword is given by $d_{\min} = n - k + 1$. The code has a capability of correcting that depends upon d_{\min} and can correct any combination of t or fewer errors, where t is expressed as

$$t = \left\lfloor \frac{d_{\min} - 1}{2} \right\rfloor = \left\lfloor \frac{n - k}{2} \right\rfloor \quad n-k \text{ is even} \quad (19)$$

$$t = \left\lfloor \frac{n - k - 1}{2} \right\rfloor \quad n-k \text{ is odd} \quad (20)$$

where $\lfloor x \rfloor$ means that the largest integer does not exceed x .

3.5.2 Hamming Codes

Hamming codes are widely employed for error control in various applications from data storage systems to on-chip micro-networks because of their implementation flexibility as well as low codec complexity [104]. When used, parity checking alone can detect errors but not correct them, but a sophisticated pattern of parity checking, called Hamming, was introduced to correct single errors along as well as detect double errors. Parity of binary bits is found by using

modulo 2 sum of the binary bits. The modulo two sum can be calculated with the help of matrices.

Hamming codes are defined by one parameter, m , which is an integer satisfying $m \geq 2$. A Hamming code (n, k) has a code length of n and message length of k , where $n = 2^m - 1$, $k = 2^m - m - 1$. Encoding and decoding of Hamming codes is achieved with the help of two matrices: the generator matrix G ($k \times n$) and the parity check H $(n-k) \times n$.

There exists a relation between G and H . If G is in the systematic format $G = [I \ P]$, then H can be calculated as $H = [P^T \ I]$ or $G = [P \ I]$, and $H = [I \ P^T]$, where I is the identity matrix of dimensions $k \times k$ and P is a matrix of dimensions $k \times (n - k)$. By knowing any one of the matrices, the other can be found using this relation. A parity check is constructed with all non-zero length- m binary words as columns. The ordering of the column is arbitrary. For example, Hamming $(7,4)$ has $m = 3$, $n = 7$, $k = 4$. All non-zero possible combinations of three-bit messages that could give the parity check matrix H :

$$H = \begin{pmatrix} 1 & 0 & 0 & 1 & 1 & 0 & 1 \\ 0 & 1 & 0 & 1 & 0 & 1 & 1 \\ 0 & 0 & 1 & 0 & 1 & 1 & 1 \end{pmatrix} \quad G = \begin{pmatrix} 1 & 1 & 0 & 1 & 0 & 0 & 0 \\ 1 & 0 & 1 & 0 & 1 & 0 & 0 \\ 0 & 1 & 1 & 0 & 0 & 1 & 0 \\ 1 & 1 & 1 & 0 & 0 & 0 & 1 \end{pmatrix}.$$

Relative to encoding, the codeword could be easily generated by matrix multiplication once the generator matrix G is known, using the relation $C = mG$, where C is the codeword vector, m is the message vector, and G is the generator matrix.

Relative to error-correction capability, the number of errors that can be corrected depends upon the minimum Hamming distance between code words: if it is “ d ,” then it can detect $d-1$ errors or correct $(d-1)/2$ errors. For a Hamming $(7,4)$ code, the minimum distance is 3, thereby correcting only a single error.

Relative to hardware implementation, the implementation of Hamming codes can be done using flip flops formed of XOR gates, which occupy a very small die area [105].

CHAPTER 4

MODELING OF PROPOSED SYSTEM

To analyze a system, elements of the system must be modeled. In this chapter, the methods adopted to model the communication and powering blocks of the bio-mote, as shown previously in Figure 7, are discussed.

4.1 Magnetic Induction Communication Model

This research adopted the power transfer model presented in the work of Sun and Akyildiz [106], which modeled a magnetic induction-based communication system with underground soil as medium. In that work, the magnetic induction transmitter and receiver have been modeled as a primary coil and the secondary coil of a transformer, respectively, which is shown as transformer model in Figure 13.

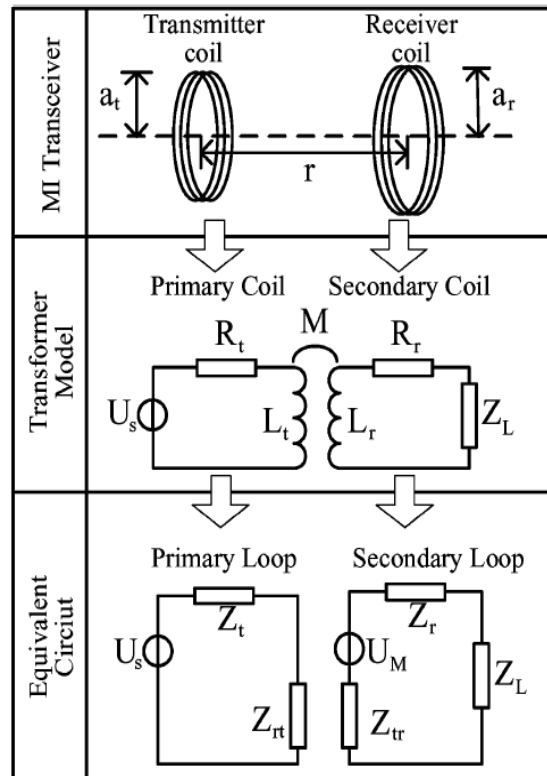


Figure 13. Modeling of channel for magnetic induction [106].

Since the effect of parasitic capacitance can be mitigated by operating at low frequency, the transformer model presented in the Figure 13 does not include the parasitic capacitance. In Figure 13, the following apply:

M = Mutual induction of transmitter coil and receiver coil

U_s = Voltage source at transmitter

a_t, a_r = Radius of transmitter and receiver coils, respectively

R_t, R_r = Resistances of coils

L_t, L_r = Self-inductance of coils

Z_L = Load impedance of receiver

In order to analyze the performance of the transformer model, the equivalent circuit of the transformer model as shown in the third row of Figure 13 is used. The values of the parameters shown in the model are as follows:

$$Z_t = R_t + j\omega L_t \quad (21)$$

$$Z_{rt} = \frac{\omega^2 M^2}{R_r + j\omega L_r + Z_L} \quad (22)$$

$$Z_r = R_r + j\omega L_r \quad (23)$$

$$Z_{tr} = \frac{\omega^2 M^2}{R_t + j\omega L_t} \quad (24)$$

$$U_M = -j\omega M \frac{U_s}{R_t + j\omega L_t} \quad (25)$$

where

Z_{rt}, Z_{tr} = Influence of receiver over transmitter, and vice versa, respectively

Z_t, Z_r = Self impedance of transmitter and receiver, respectively.

U_s = Induced voltage on receiver side

The transmitted power on the transmitter side is equal to the amount of power consumed by the primary loop, and the amount of power received at the receiver is equal to the amount of power consumed by the load impedance Z_L . The transmitted and received power can be calculated using

$$P_r(r) = \text{Re} \left\{ \frac{Z_L \cdot U_M^2}{(Z_r' + Z_r + Z_L)^2} \right\} \quad (26)$$

$$P_t(r) = \text{Re} \left\{ \frac{U_s^2}{Z_t' + Z_t} \right\} \quad (27)$$

Since the main aim here is to transfer the maximum possible power to the secondary side, transmission line theory was used in order to achieve it. According to transmission line theory, the maximum power can be transferred to the receiver side using impedance matching techniques. Here, the matching impedance on the receiver side can be achieved by making the load impedance equal to the complex conjugate of the output impedance of the receiver, which is given by

$$Z_L = \overline{Z_r + Z_r'}$$

In order to calculate the power received at the receiver the resistances (R_t , R_r), the self-inductances (L_t , L_r) of coils should be known, which are calculated using the following expressions:

$$R_t = N_t \cdot 2\pi a_t \cdot R_0 \quad (28)$$

$$R_r = N_r \cdot 2\pi a_r \cdot R_0 \quad (29)$$

$$L_t = \frac{1}{2} \mu\pi N_t^2 a_t \quad (30)$$

$$L_r = \frac{1}{2} \mu\pi N_r^2 a_r \quad (31)$$

where $\mu = 4\pi \times 10^{-7}$, and R_0 is the resistance of a unit length of the coil.

The mutual inductance is a measure of the total flow of magnetic flux from one current-carrying path that passes through another closed path and represents how well the primary and secondary coils are coupled. Therefore, a high value of mutual induction represents a higher voltage being induced on the secondary side. Mutual induction is one of the most important parameters when it comes to power transfer using magnetic induction. The mutual inductance is calculated using

$$M = \frac{\mu\pi N_t N_r a_t^2 a_r^2}{2r^3} \quad (32)$$

According to equation (31), the voltage induced is largely dependent upon the geometry of the coils and the distance between them.

Path loss is defined using the transmitted and received power as

$$PL = -10 \lg \frac{P_r(r)}{P_t} \quad (33)$$

where $P_r(r)$ is the received power at a distance of r meters.

4.2 Ultrasound Powering Model

For this research, a powering model presented in the work of Jornet, J.M., and Akyildiz, I.F. [107] is been utilized, which uses ZnO nanowires was adopted [108, 109]. The presented model uses a vibration-harvesting technique using piezoelectric device. In contrast to the previous statement, the disadvantage of a location-specific application, is that the present device has the potential of harvesting energy from various sources: mechanical (such as body movement, muscle stretching, blood pressure), vibration energy (such as acoustic/ultrasonic waves), and hydraulic energy (such as flow of body fluids, blood flow, contraction of blood

vessels, dynamic fluid in nature) [112], thus making it location independent.

In the work of Jornet and Akyildiz [107], realistic values of energy capacity and the energy-harvesting rate are calculated using an analytical model that captures various aspects of the harvesting process, such as capabilities and limitations using piezoelectric nanogenerators. The model shown in Figure 14 consists of an ideal voltage source V_g , which is equal to the difference of the electrostatic potential of the bent wire and voltage across the rectifying circuits.

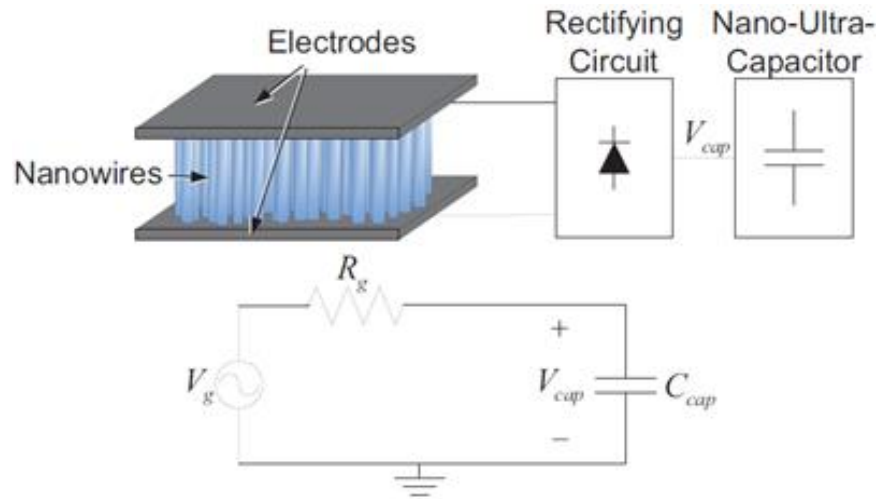


Figure 14. Nanogenerator using ZnO nanowires along with rectifying circuit that can store energy in a capacitor (top) and its equivalent model (bottom) [107].

In Figure 14, resistance $R_g = V_g / I_g$. The term I_g is the current generated by the nanogenerator and is defined as the amount of energy harvested for a unit compress-release cycle of a nanowire. If the ΔQ is the harvested charge for cycle length t_{cycle} , then I_g can be calculated as

$$I_g = \Delta Q / t_{cycle}. \quad (34)$$

The capacitor voltage as a function of number of cycles n_{cycle} can be calculated as

$$\begin{aligned} V_{\text{cap}}(n_{\text{cycle}}) &= V_g \left(1 - e^{\left(-\frac{n_{\text{cycle}} t_{\text{cycle}}}{R_g C_{\text{cap}}} \right)} \right) \\ &= V_g \left(1 - e^{\left(-\frac{n_{\text{cycle}} \Delta Q}{V_g C_{\text{cap}}} \right)} \right) \end{aligned} \quad (35)$$

where C_{cap} is the total capacitance of the nano capacitor. The energy stored in the capacitor E_{cap} as a function of the number of cycles n_{cycle} can found using

$$E_{\text{cap}}(n_{\text{cycle}}) = \frac{1}{2} C_{\text{cap}} (V_{\text{cap}}(n_{\text{cycle}}))^2 \quad (36)$$

The maximum energy that can be stored by the nano-capacitor is given by

$$E_{\text{cap-max}} = \max \{ E_{\text{cap}}(n_{\text{cycle}}) \} = \frac{1}{2} C_{\text{cap}} V_g^2 \quad (37)$$

The number of cycles required to charge the capacitor to a value E is

$$n_{\text{cycle}}(E) = \left| -\frac{V_g C_{\text{cap}}}{\Delta Q} \ln \left(1 - \sqrt{\frac{2E}{C_{\text{cap}} V_g^2}} \right) \right| \quad (38)$$

Using a value of $\Delta Q = 6\text{pC}$, which was achieved on a dimension of $1000 \mu\text{m}^2$ [110] and using an ultra nano-capacitor with $C_{\text{cap}} = 9\text{nF}$ of nanosize dimensions [111]. Using the above equations (35), (36), and (37), the maximum amount of energy that was calculated was approximately 800 pJ when C_{cap} was charged at $V_g = 0.42 \text{ V}$, which needs approximately 2500 cycles.

From the above model, it is calculated that with the maximum energy harvested, the capacitor can be charged up to 0.42 V. Therefore, using this model for the remaining analysis, it

is assumed that 0.4 V is available at the bio-mote. Figure 15 shows that that the analytical model presented in this chapter matches the measurement of the actual device reported in [109]

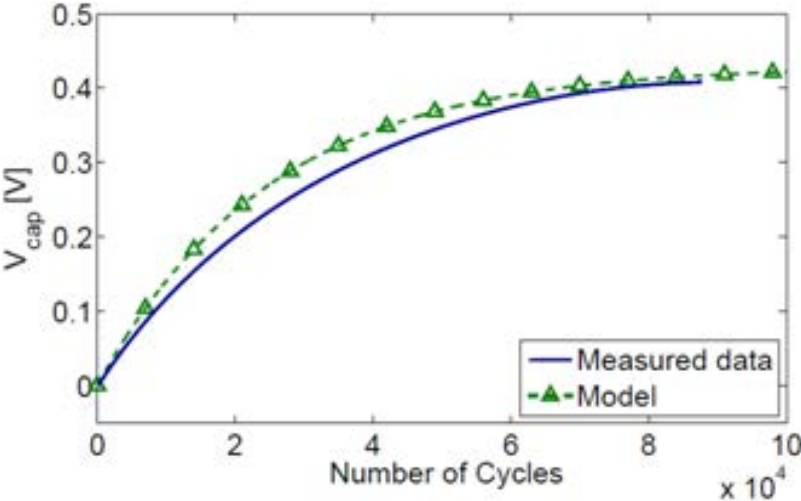


Figure 15. Comparison between actual device and model by measuring amount of voltage generated as function of number cycles of ultrasound [107]

CHAPTER 5

RESULTS

5.1 Introduction

The magnetic induction-based model along with the ultrasound model, as explained in Chapter 4, was simulated in MATLAB using the design parameters shown in Table 6. This chapter presents the results which were achieved through the simulations.

TABLE 6

DIFFERENT PARAMETER VALUES USED TO CALCULATE PERFORMANCE OF BIO-MOTE

Parameter	Value
External Coil Radius	5 cm
Channel	Additive White Gaussian Noise
Implant Coil Radius	30 μm
Noise Power	-80 db
Carrier Frequency	13.56 Mhz
Magnetic Permeability	1
Side Band Attenuation	40 db

5.2 Voltage Induced

The amount of voltage induced in the external reader given that 0.4 V is available at the bio-mote is shown in Figure 16. As can be seen, using the proposed system, a voltage in the range of a few milli volts can be induced in the external reader (cell phone).

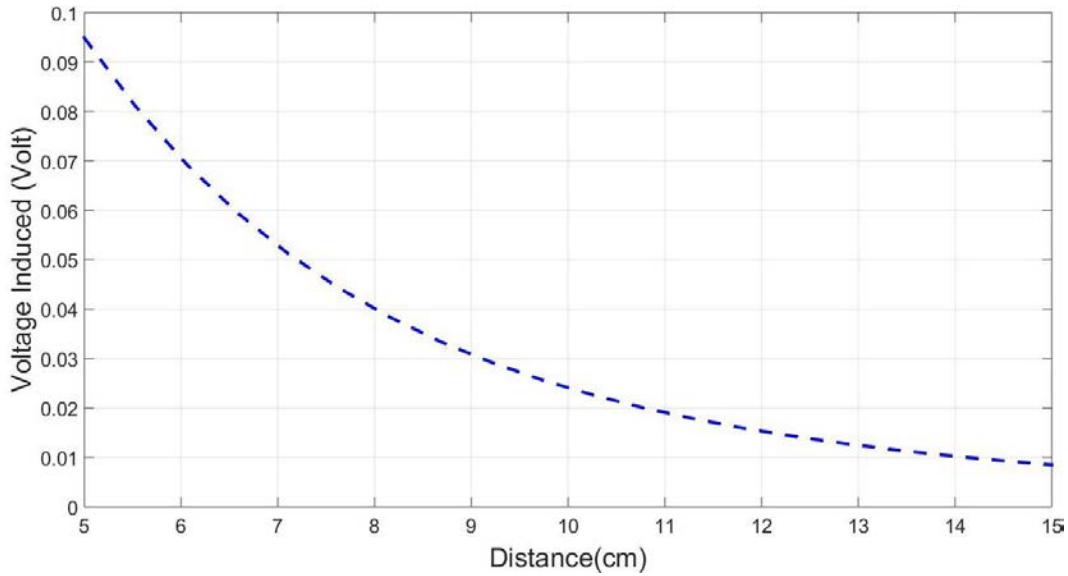


Figure 16. Voltage induced in external coil due to bio-mote with respect to distance separating bio-mote and external coil (cell phone).

5.3 Power Induced

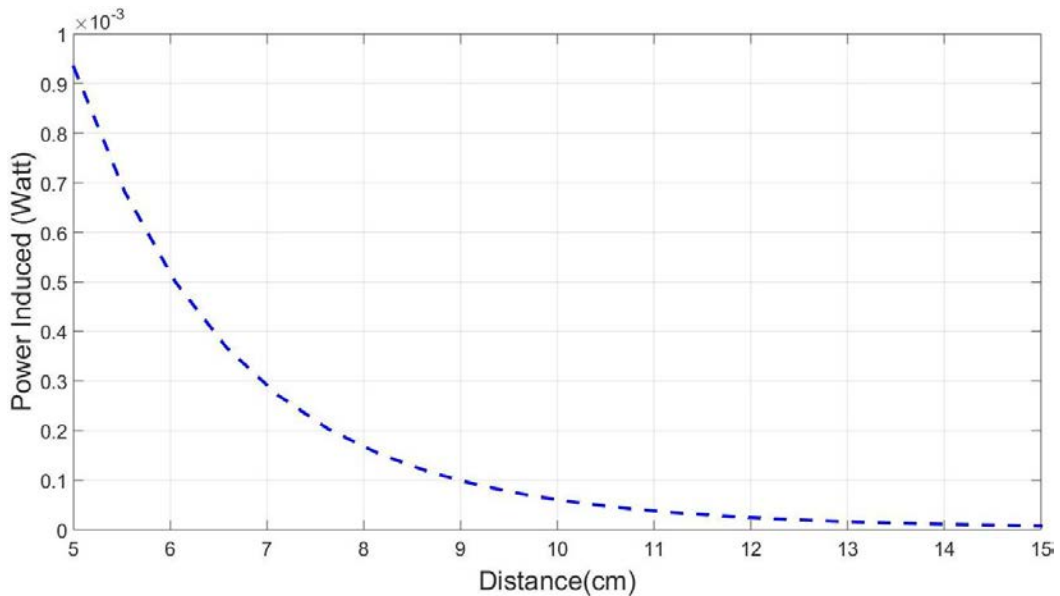


Figure 17. Power induced in external coil due to bio-mote with respect to distance separating bio-mote and external coil (mobile phone)

The amount of power induced by the bio-mote at the receiver with respect to the distance between bio-mote and the external device is shown in Figure 17. Given a receiver sensitivity of -120 dBm the signal can be detected by the receiver (cell phone).

5.4 BER Performance Using Error-Correction and Modulation

5.4.1 Comparison of BPSK Using Hamming vs BPSK Using RS Codes

The performance of the two systems in terms of BER using BPSK alongside Hamming, and BPSK alongside RS codes is compared in Figure 18. The graph shows that both systems tend to deliver the same performance after 6 cm. For distance less than 6 cm, RS codes perform better than hamming codes but their performance becomes closer as the distance increases. For wireless communication, the acceptable BER is in the range of 10^{-3} - 10^{-8} depending upon the data rate (20 kbps – 100 Mbps) [113]. Given the acceptable BER, the maximum performance that could be achieved in terms of distance (communication range) occurs between 5 cm and 6 cm.

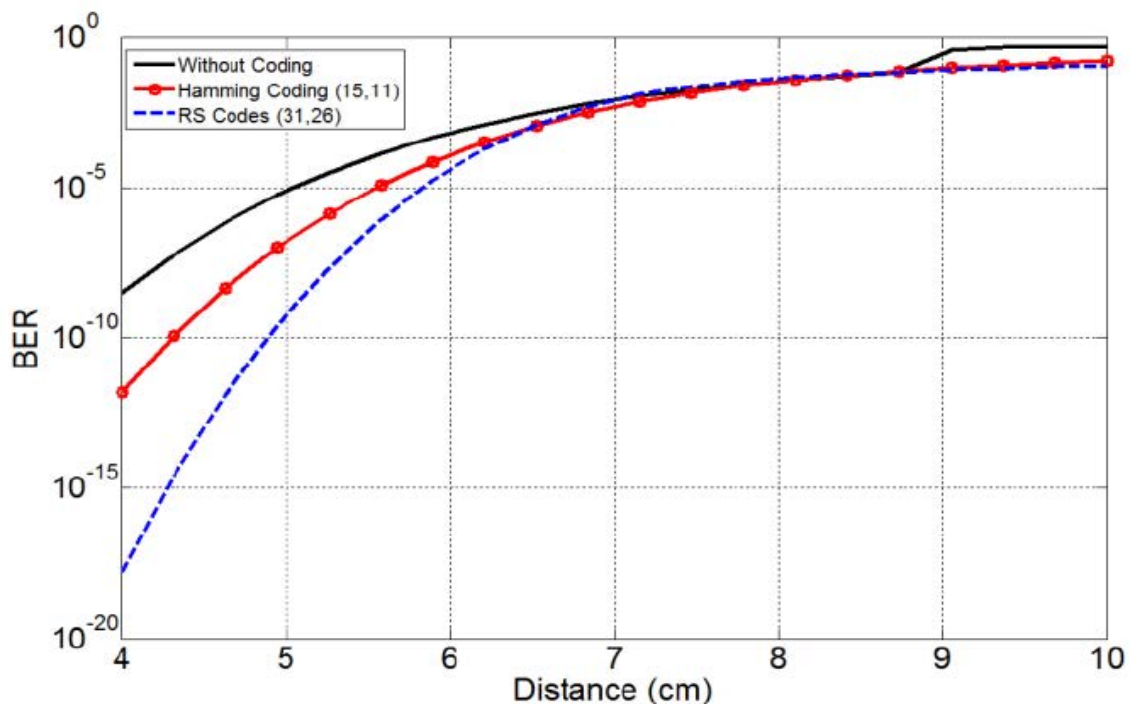


Figure 18. BER for various distances between external device and bio-mote using BPSK modulation.

5.4.2 Comparison of ASK Using Hamming vs ASK Using RS Codes

The performance of the two systems in terms of BER using ASK alongside Hamming,

and ASK alongside RS codes is compared in Figure 19. This graph shows that the performance of both systems tends to be the same after a distance of 5 cm. For distances less than 6 cm, RS codes perform better than Hamming codes, but their performance becomes closer as the distance increases. Given the acceptable BER, the maximum performance that could be achieved in terms of distance (communication range) occurs between 4 cm and 5 cm.

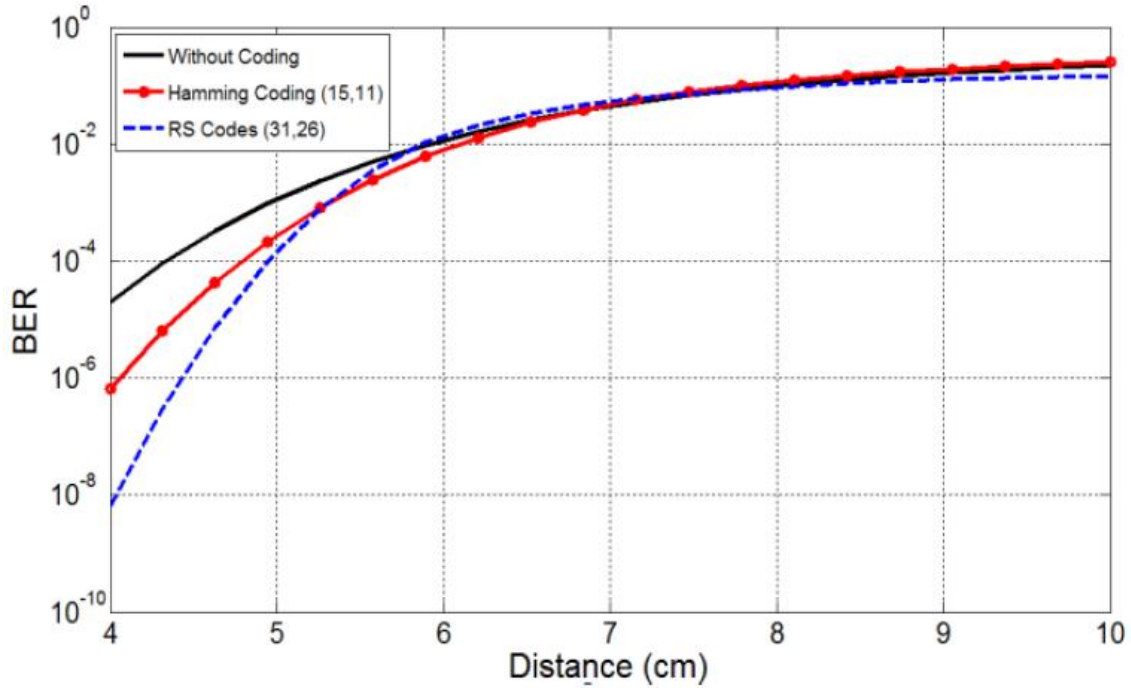


Figure 19. BER for various distances between external device and bio-mote using ASK modulation.

5.5 Conclusion

From Figures 18 and 19, it can be seen that a communication range in centimeters is achievable depending upon the required BER. When comparing the performance with respect to both modulation and error-correction coding, BPSK along with RS codes performs the best. Various implants require different BERs, depending upon the format of data transmitted (e.g., image, video). Once the required BER is known, then the respective combination of modulation and error coding can be used according to the graphs. Since power and voltage in the order of

few mV and μ W can be induced in the external device such as cell phone, it can be said that the signal sent from the bio-mote can be detectable at the external device. Depending upon the sensitivity of the receiver, the communication range of the bio-mote can be determined.

CHAPTER 6

CONCLUSION

Designing wireless sensors at micro scale could prove helpful in healthcare giving the ability for individuals to continuously monitor their body. To transmit data wirelessly from a sensor, present inside the human body to an external device such as a mobile phone the communication range of the sensor should be in centimeters. In most methods adopted by various works presented in the literature review section of this work, the communication range is limited to millimeter and the papers which reached few centimeters increased the device size to centimeters. To achieve a communication range in centimeters while keeping the device size in micrometers, we have proposed a hybrid model with error control coding techniques. A system model was developed that integrates the proposed methods with the traditional communication system of a sensor. Bit error rate (BER) is used as a performance measure. BER for various combinations of modulation and error control coding techniques were compared using MATLAB to find the best combination for the proposed system. With a target BER in the range of 10^{-3} to 10^{-8} , it was observed that the proposed system could achieve a maximum communication range of 5 cm.

In the future, high quality factor and biocompatible inductive coils at nano or micro size would be introduced to further improve the communication range and to make the sensor more real time applicable. We would also like to evaluate the performance of a network of such devices. Anti-collision and positioning techniques would be introduced in order to enable the external device (mobile phone) to read the data from multiple bio-motes and in order to know the source (heart, brain etc.) of the received data at the external device respectively.

REFERENCES

REFERENCES

- [1] Haertling, G.H., 1999. Ferroelectric ceramics: History and technology. *Journal of the American Ceramic Society*, 82(4), pp. 797-818.
- [2] Wang, Z.L., and Wu, W., 2012. Nanotechnology-enabled energy harvesting for self-powered micro- /nanosystems. *Angewandte Chemie International Edition*, 51(47), pp.11700-11721.
- [3] Amar, A.B., Kouki, A.B., and Cao, H., 2015. Power approaches for implantable medical devices. *Sensors*, 15(11), pp. 28889-28914.
- [4] Cadei, A., Dionisi, A., Sardini, E., and Serpelloni, M., 2013. Kinetic and thermal energy harvesters for implantable medical devices and biomedical autonomous sensors. *Measurement Science and Technology*, 25(1), 14 pp.
- [5] Mitcheson, P.D., Yeatman, E.M., Rao, G.K., Holmes, A.S., and Green, T.C., 2008. Energy harvesting from human and machine motion for wireless electronic devices. *Proceedings IEEE*, 96(9), pp. 1457-1486.
- [6] Liu, J.Q., Fang, H.B., Xu, Z.Y., Mao, X.H., Shen, X.C., Chen, D., Liao, H., and Cai, B.C., 2008. A MEMS-based piezoelectric power generator array for vibration energy harvesting. *Microelectronics Journal*, 39(5), pp. 802-806.
- [7] Wang, Z.L., 2012. From nanogenerators to piezotronics: A decade-long study of ZnO nanostructures. *MRS Bulletin*, 37(9), pp. 814-827.
- [8] Deterre, M., Lefevre, E., and Dufour-Gergam, E., 2012. An active piezoelectric energy extraction method for pressure energy harvesting. *Smart Materials and Structures*, 21(8), 9 pp.
- [9] Sue, C.-Y., and Tsai, N.-C., 2012. Human powered MEMS-based energy harvest devices. *Applied Energy*, 93, pp. 390-403.
- [10] Beeby, S.P., Tudor, M.J., and White, N.M., 2006. Energy harvesting vibration sources for microsystems applications. *Measurement Science and Technology*, 17, pp. 175-195.
- [11] Selvarathinam, J., and Anpalagan, A., 2016. Energy harvesting from the human body for biomedical applications. *IEEE Potentials*, 35(6), pp. 6-12.
- [12] Jo, S.E., Kim, M.K., Kim, M.S., and Kim, Y.J., 2012. Flexible thermoelectric generator for human body heat energy harvesting. *Electronics Letters*, 48(16), pp. 1013-1015.

REFERENCES (continued)

- [13] Amar, A.B., Kouki, A.B., and Cao, H., 2015. Power approaches for implantable medical devices. *Sensors*, 15(11), pp. 28889-28914.
- [14] Murakawa, K., Kobayashi, M., Nakamura, O., and Kawata, S., 1999. A wireless near-infrared energy system for medical implants. *IEEE Engineering in Medicine and Biology Magazine*, 18(6), pp. 70-72.
- [15] Mujeeb-U-Rahman, M., Adalian, D., Chang, C.F., and Scherer, A., 2015. Optical power transfer and communication methods for wireless implantable sensing platforms. *Journal of biomedical optics*, 20(9), p. 095012.
- [16] Ayazian, S., and Hassibi, A., August. Delivering optical power to subcutaneous implanted devices. *2011 Annual International Conference of the IEEE in Engineering in Medicine and Biology Society*, pp. 2874-2877.
- [17] Larson, B.C., 1999. An optical telemetry system for wireless transmission of biomedical signals across the skin (doctoral dissertation, Massachusetts Institute of Technology).
- [18] Aktan, O., Sarioglu, B., Cindemir, U., Ünlü, S.O., Dündar, G., Mutlu, Ş., and Yalcinkaya, A.D., 2011. Optoelectronic CMOS power supply unit for electrically isolated microscale applications. *IEEE Journal of Selected Topics in Quantum Electronics*, 17(3), pp.747-756.
- [19] Haydaroglu, I., and Mutlu, S., 2015. Optical power delivery and data transmission in a wireless and batteryless microsystem using a single light emitting diode. *Journal of Microelectromechanical Systems*, 24(1), pp.155-165.
- [20] Ayazian, S., and Hassibi, A. Delivering optical power to subcutaneous implanted devices. *2011 Annual International Conference of the IEEE in Engineering in Medicine and Biology Society*, pp. 2874-2877.
- [21] Ayazian, S., Akhavan, V.A., Soenen, E., and Hassibi, A., 2012. A photovoltaic-driven and energy-autonomous CMOS implantable sensor. *IEEE Transactions on Biomedical Circuits and Systems*, 6(4), pp. 336-343.
- [22] Schanze, T., Hesse, L., Lau, C., Greve, N., Haberer, W., Kammer, S., Doerge, T., Rentzos, A., and Stieglitz, T., 2007. An optically powered single-channel stimulation implant as test system for chronic biocompatibility and biostability of miniaturized retinal vision prostheses. *IEEE Transactions on Biomedical Engineering*, 54(6), pp. 983-992.

REFERENCES (continued)

- [23] Laflin, K.E., Morris, C.J., Bassik, N., Jamal, M., and Gracias, D.H., 2011. Tetherless microgrippers with transponder tags. *Journal of Microelectromechanical Systems*, 20(2), pp. 505-511.
- [24] Mujeeb-U-Rahman, M., Adalian, D., Chang, C.F., and Scherer, A., 2015. Optical power transfer and communication methods for wireless implantable sensing platforms. *Journal of biomedical optics*, 20(9), p. 095012.
- [25] Charthad, J., Weber, M.J., Chang, T.C., and Arbabian, A., 2015. A mm-sized implantable medical device (IMD) with ultrasonic power transfer and a hybrid bi-directional data link. *IEEE Journal of Solid-State Circuits*, 50(8), pp. 1741-1753.
- [26] Davilis, Y., Kalis, A., and Ifantis, A., 2010. On the use of ultrasonic waves as a communications medium in biosensor networks. *IEEE Transactions on Information Technology in Biomedicine*, 14(3), pp. 650-656.
- [27] Galluccio, L., Melodia, T., Palazzo, S., and Santagati, G.E., January 2012. Challenges and implications of using ultrasonic communications in intra-body area networks. *9th Annual Conference on Wireless On-Demand Network Systems and Services*, pp. 182-189.
- [28] Akyildiz, I.F., Pompili, D., and Melodia, T., 2005. Underwater acoustic sensor networks: Research challenges. *Ad Hoc Networks*, 3(3), pp. 257-279.
- [29] Denisov, A., and Yeatman, E., June 2010. Ultrasonic vs. inductive power delivery for miniature biomedical implants. *2010 International Conference on Body Sensor Networks*, pp. 84-89.
- [30] Santagati, G.E., and Melodia, T., 2017. Experimental evaluation of impulsive ultrasonic intra-body communications for implantable biomedical devices. *IEEE Transactions on Mobile Computing*, 16(2), pp. 367-380.
- [31] Galluccio, L., Melodia, T., Palazzo, S., and Santagati, G.E., January 2012. Challenges and implications of using ultrasonic communications in intra-body area networks. *2012 9th Annual Conference on Wireless On-demand Network Systems and Services*, pp. 182-189.
- [32] Federal Communications Commission, August 1996. Guidelines for evaluating the environmental effects of radiofrequency radiation, FCC, Washington, DC.
- [33] IEEE Standards Coordinating Committee, 1992. IEEE standard for safety levels with respect to human exposure to radio frequency electromagnetic fields, 3 kHz to 300 GHz.

REFERENCES (continued)

- [34] Szabo, T. L., 2004. *Diagnostic Ultrasound Imaging: Inside Out*. Elsevier, Inc., London.
- [35] Basak, A., Ranganathan, V., and Bhunia, S., 2014. Implantable ultrasonic imaging assembly for automated monitoring of internal organs. *IEEE Transactions on Biomedical Circuits and Systems*, 8(6), pp. 881-890.
- [36] Seo, D., Carmena, J.M., Rabaey, J.M., Alon, E., and Maharbiz, M.M., 2013. Neural dust: An ultrasonic, low power solution for chronic brain-machine interfaces. arXiv preprint, pp. 1307-2196. SAME AS [51]
- [37] Arra, S., Leskinen, J., Heikkila, J., and Vanhala, J., February 5-7, 2007. Ultrasonic power and data link for wireless implantable applications. *IEEE 2nd International Symposium on Wireless Pervasive Computing*.
- [38] Roes, M.G., Duarte, J.L., Hendrix, M.A., and Lomonova, E.A., 2013. Acoustic energy transfer: A review. *IEEE Transactions on Industrial Electronics*, 60(1), pp. 242-248.
- [39] Sanni, A., Vilches, A., and Toumazou, C., 2012. Inductive and ultrasonic multi-tier interface for low-power, deeply implantable medical devices. *IEEE Transactions on Biomedical Circuits and Systems*, 6(4), pp. 297-308.
- [40] Davilis, Y., Kalis, A., and Ifantis, A., 2010. On the use of ultrasonic waves as a communications medium in biosensor networks. *IEEE Transactions on Information Technology in Biomedicine*, 14(3), pp. 650-656.
- [41] Lee, K.L., Lau, C.-P., Tse, H.-F., Echt, D.S., Heaven, D., Smith, W., and Hood, M., 2007. First human demonstration of cardiac stimulation with transcutaneous ultrasound energy delivery. *Journal of the American College of Cardiology*, 50(9), pp. 877-883.
- [42] Charthad, J., Weber, M.J., Chang, T.C., and Arbabian, A., 2015. A mm-sized implantable medical device (IMD) with ultrasonic power transfer and a hybrid bi-directional data link. *IEEE Journal of Solid-State Circuits*, 50(8), pp. 1741-1753.
- [43] Meng, M., and Kiani, M., 2017. Design and optimization of ultrasonic wireless power transmission links for millimeter-sized biomedical implants. *IEEE Transactions on Biomedical Circuits and Systems*, 11(1), pp. 98-107.
- [44] Mazzilli, F., Lafon, C., and Dehollain, C., 2014. A 10.5 cm ultrasound link for deep implanted medical devices. *IEEE Transactions on Biomedical Circuits and Systems*, 8(5), pp. 738-750.

REFERENCES (continued)

- [45] Tsai, J.Y., Huang, K.H., Wang, J.R., Liu, S.I., and Li, P.C., October 2011. Ultrasonic wireless power and data communication for neural stimulation. *2011 IEEE International Ultrasonics Symposium*, pp. 1052-1055
- [46] Cotté, B., Lafon, C., Dehollain, C., and Chapelon, J.-Y., 2012. Theoretical study for safe and efficient energy transfer to deeply implanted devices using ultrasound. *IEEE Transactions on Ultrasonics, Ferroelectrics, and Frequency Control*, 59(8), 59.8, pp. 1674-1685.
- [47] Rosa, B.M., and Yang, G.Z., June 2016. Active implantable sensor powered by ultrasounds with application in the monitoring of physiological parameters for soft tissues. *IEEE 13th International Conference on Wearable and Implantable Body Sensor Networks*, pp. 318-323.
- [48] Ozeri, S., and Shmilovitz, D., 2014. Simultaneous backward data transmission and power harvesting in an ultrasonic transcutaneous energy transfer link employing acoustically dependent electric impedance modulation. *Ultrasonics*, 54(7), pp. 1929-1937.
- [49] Galluccio, L., Melodia, T., Palazzo, S., and Santagati, G.E., January 2012. Challenges and implications of using ultrasonic communications in intra-body area networks. *2012 9th Annual Conference on Wireless On-Demand Network Systems and Services*, pp. 182-189.
- [50] Ergun, A. S., Yaralioglu, G.G., and Khuri-Yakub, B.T., 2003. Capacitive micromachined ultrasonic transducers: Theory and technology. *Journal of Aerospace Engineering*, 16(2), pp. 76-84.
- [51] Banerji, S., Goh, W.L., Cheong, J.H., and Je, M., December 2013. CMUT ultrasonic power link front-end for wireless power transfer deep in body. *2013 IEEE MTT-S International Microwave Workshop Series on RF and Wireless Technologies for Biomedical and Healthcare Applications*, pp. 1-3.
- [52] Lockwood, G.R., Turnbull, D.H., Christopher, D.A. and Foster, F.S., 1996. Beyond 30 MHz [applications of high-frequency ultrasound imaging]. *IEEE Engineering in Medicine and Biology Magazine*, 15(6), pp. 60-71.
- [53] Smith, R., Arca, A., Chen, X., Marques, L., Clark, M., Aylott, J., and Somekh, M., 2012. Design and fabrication of nanoscale ultrasonic transducers. *Journal of Physics: Conference Series*, 353(1), p. 012001).

REFERENCES (continued)

- [54] Cannata, J.M., Ritter, T.A., Chen, W.-H., Silverman, R.H., and Shung, K.K., 2003. Design of efficient, broadband single-element (20-80 MHz) ultrasonic transducers for medical imaging applications. *IEEE Transactions on Ultrasonics, Ferroelectrics, and Frequency Control*, 50(11), pp. 1548-1557.
- [55] Yoon, S., Kim, M.G., Williams, J.A., Yoon, C., Kang, B.J., Cabrera-Munoz, N., Shung, K.K., and Kim, H.H., 2015. Dual-element needle transducer for intravascular ultrasound imaging. *Journal of Medical Imaging*, 2(2), p. 027001.
- [56] Liu, C., Djuth, F.T., Zhou, Q., and Shung, K.K., 2013. Micromachining techniques in developing high-frequency piezoelectric composite ultrasonic array transducers. *IEEE Transactions on Ultrasonics, Ferroelectrics, and Frequency Control*, 60(12), pp. 2615-2625.
- [57] Lu, Y., and Horsley, D.A., 2015. Modeling, fabrication, and characterization of piezoelectric micromachined ultrasonic transducer arrays based on cavity SOI wafers. *Journal of Microelectromechanical Systems*, 24(4), pp. 1142-1149.
- [58] Zhou, Q., Lam, K.H., Zheng, H., Qiu, W., and Shung, K.K., 2014. Piezoelectric single crystal ultrasonic transducers for biomedical applications. *Progress in Materials Science*, 66, pp. 87-111.
- [59] Shung, K.K., Cannata, J.M., and Zhou, Q.F., 2007. Piezoelectric materials for high frequency medical imaging applications: A review. *Journal of Electroceramics*, 19, pp. 139-45.
- [60] Przybyla, R.J., Shelton, S.E., Guedes, A., Izyumin, I.I., Kline, M.H., Horsley, D.A., and Boser, B.E., 2011. In-air rangefinding with an AlN piezoelectric micromachined ultrasound transducer. *IEEE Sensors Journal*, 11(11), pp. 2690-2697.
- [61] Ronan, P., 2015. EM spectrum. URL: https://commons.wikimedia.org/wiki/File:EM_spectrum.svg [11/21/2017].
- [62] Zhu, B., Li, J., Hu, W. and Gao, X., 2015. Review of magnetic coupling resonance wireless energy transmission. *International Journal of u- and e- Service, Science and Technology*, 8(3), pp. 257-272.
- [63] Wikipedia, 2017. Near and far field. URL: https://en.wikipedia.org/wiki/Near_and_far_field [11/21/2017].
- [64] Occhiuzzi, C., Contri, G., and Marrocco, G., 2012. Design of implanted RFID tags for passive sensing of human body: The STENTag. *IEEE Transactions on Antennas and Propagation*, 60(7), pp. 3146-3154.

REFERENCES (continued)

- [65] Hervé, A., 2011. RFID technology for human implant devices. *Comptes Rendus Physique*, 12(7), pp. 675-683.
- [66] Burke, P., and Rutherglen, C., 2010. Towards a single-chip, implantable RFID system: Is a single-cell radio possible? *Biomedical Microdevices*, 12(4), pp. 589-596.
- [67] Lu, C.-H., Li, J.-A. and Lin, T.-H., 2016. A 13.56-MHz passive NFC tag IC in 0.18- μm CMOS process for biomedical applications. *2016 International Symposium on VLSI Design, Automation and Test*, pp. 1-4.
- [68] Ho, J.S., Yeh, A.J., Neofytou, E., Kim, S., Tanabe, Y., Patiolla, B., Beygui, R.E., and Poon, A.S.Y., 2014. Wireless power transfer to deep-tissue micro implants. *Proceedings National Academy of Sciences*, 111(22), pp. 7974-7979.
- [69] Freitas Jr., R.A., 1999. *Nanomedicine, Volume I: Basic Capabilities*. Landes Bioscience, Austin, TX.
- [70] Jow, U.-M., and Ghovanloo, M., 2009. Modeling and optimization of printed spiral coils in air, saline, and muscle tissue environments. *IEEE Transactions on Biomedical Circuits and Systems*, 3(5), pp. 339-347.
- [71] Lenaerts, B., and Puers, R., 2007. An inductive power link for a wireless endoscope. *Biosensors and Bioelectronics*, 22(7), pp. 1390-1395.
- [72] Xue, R.-F., Cheng, K.-W., and Je, M., 2013. High-efficiency wireless power transfer for biomedical implants by optimal resonant load transformation. *IEEE Transactions on Circuits and Systems I: Regular Papers*, 60(4), pp. 867-874.
- [73] RamRakhyani, A.K., Mirabbasi, S., and Chiao, M., 2011. Design and optimization of resonance-based efficient wireless power delivery systems for biomedical implants. *IEEE Transactions on Biomedical Circuits and Systems*, 5(1), pp. 48-63.
- [74] Kim, Sanghoek, John S. Ho, and Ada SY Poon. Midfield wireless powering of subwavelength autonomous devices. *Physical review letters* 110.20,2013, pp. 203-905.
- [75] Karalis, Aristeidis, John D. Joannopoulos, and Marin Soljačić. Efficient wireless non-radiative mid-range energy transfer. *Annals of Physics* 323.1,2008, pp. 34-48.
- [76] Akyildiz, I. F., Jornet, J.M., and Han, C., 2014. Terahertz band: Next frontier for wireless communications. *Physical Communication*, 12, pp. 16-32.

REFERENCES (continued)

- [77] Hassouni, S., and Qjidaa, H., 2015. A design of modulator and demodulator for a passive UHF RFID tag using DTMOST compatible with C1 G2 EPC standard protocol. *International Journal of Wireless Information Networks*, 22(4), pp. 407-414.
- [78] Muller, R., Le, H.P., Li, W., Ledochowitsch, P., Gambini, S., Bjorninen, T., Koralek, A., Carmena, J.M., Maharbiz, M.M., Alon, E., and Rabaey, J.M., 2015. A minimally invasive 64-channel wireless μ ECoG implant. *IEEE Journal of Solid-State Circuits*, 50(1), pp. 344-359.
- [79] Yeknami, A.F., 2014. Low-power delta-sigma modulators for medical applications (dissertation no. 1563, Department of Electrical Engineering, Linköpings universitet, Sweden).
- [80] Huang, C.-C. Chen, C.-L., and Wang, C.-C., November 24-25, 2008. R-less and C-less self-sampled ASK demodulator for lower ISM band applications. *International SoC Design Conference*, 11, pp. 281-284.
- [81] Naghmouchi, F., Ghorbel, M., Hamida, A., and Samet, M., 2004. CMOS ASK system modulation dedicated to cochlear prosthesis. *IEEE First International Symposium on Control, Communications and Signal Processing*, pp. 267-270.
- [82] Zhang, F., Stoneback, M.A., and Otis, B.P., 2011. A 23 a RF-powered transmitter for biomedical applications. *IEEE Radio Frequency Integrated Circuits Symposium*, pp. 1-4
- [83] Zhu, K., Haider, M.R., Yuan, S., and Islam, S.K., 2010. A sub-1 μ a low-power FSK modulator for biomedical sensor circuits. *IEEE Computer Society Annual Symposium on VLSI*, pp. 265-268.
- [84] Gong, C.-S.A., Yao, K.-W., Shiue, M.-T., Lin, P.-Y., and Huang, C.-N., 2008. A miniaturized PSK demodulation device for short-range wireless neural prosthetic systems. *IEEE 2nd International Conference on Bioinformatics and Biomedical Engineering*, pp. 1565-1568.
- [85] Lee, S.-Y., Cheng, C.-J., and Liang, M.-C., 2011. A low-power bidirectional telemetry device with a near-field charging feature for a cardiac microstimulator. *IEEE Transactions on Biomedical Circuits and Systems*, 5(4), pp. 357–367.
- [86] Lee, Y., 2003. Antenna circuit design for RFID applications. Microchip Technology Inc., 50 pp.
- [87] Senjuti, S., 2013. Design and optimization of efficient wireless power transfer links for implantable biotelemetry systems (thesis, The University of Western Ontario, Canada).

REFERENCES (continued)

- [88] Yu, Q., and Holmes, T.W., 1999. Stray capacitance modeling of inductors by using the finite element method. *IEEE International Symposium on Electromagnetic Compatibility, 1*, pp. 305-310.
- [89] Zhou, Q., Cha, J.H., Huang, Y., Zhang, R., Cao, W., and Shung, K.K., 2009. Alumina/epoxy nanocomposite matching layers for high-frequency ultrasound transducer application. *IEEE Transactions on Ultrasonics, Ferroelectrics, and Frequency Control*, 56(1), pp. 213-219.
- [90] Tiefensee, F., and Becker-Willinger, C., September 20-23, 2009. Nanocomposite materials for high frequency ultrasound matching layers. *Proceedings 2009 IEEE Ultrasonics Symposium*, pp. 1719–21.
- [91] Wang, H., Ritter, T.A., Cao, W., and Shung, K.K., February 1999. Passive materials for high frequency ultrasonic transducers. *Proceedings SPIE Conference on Ultrasonic Transducer Engineering*, pp. 35-42.
- [92] Krimholtz, R., Leedom, D., and Matthaei, G., 1970. New equivalent circuits for elementary piezoelectric transducers. *Electronic Letters*, 6(13), pp. 398–9.
- [93] He, P., 1998. Simulation of ultrasound pulse propagation in lossy media obeying a frequency power law. *IEEE Transactions on Ultrasonics, Ferroelectrics, and Frequency Control*, 45(1), pp. 114-125.
- [94] Cheung, A.Y., and Neyzari, A., 1984. Deep local hyperthermia for cancer therapy: External electromagnetic and ultrasound techniques. *Cancer Research*, 44(1), pp. 4736s-4744s.
- [95] Hill, C.R., 1979. Ultrasonic attenuation and scattering by tissues. In *Handbook of Clinical Ultrasound*, pp. 91-98.
- [96] Santagati, G.E., Melodia, T., Galluccio, L., and Palazzo, S., 2013. Ultrasonic networking for e-health applications. *IEEE Wireless Communications*, 20(4), pp. 74-81.
- [97] Santagati, G.E., and Melodia, T., April 27-May 2, 2014. Sonar inside your body: Prototyping ultrasonic intra-body sensor networks. *2014 Proceedings IEEE Conference on Computer Communications*, pp. 2679-2687.
- [98] Kaye, G.W.C., and Laby, T.H., 1921. *Tables of Physical and Chemical Constants and Some Mathematical Functions*. New York: Longmans, Green and Company.

REFERENCES (continued)

- [99] Cotte, B., Lafon, C., Dehollain, C., and Chapelon, J.Y., 2012. Theoretical study for safe and efficient energy transfer to deeply implanted devices using ultrasound. *IEEE Transactions on Ultrasonics, Ferroelectrics, and Frequency Control*, 59(8), pp. 1674-1685.
- [100] Xiong, F., Xiong, F., and Xiong, F., 2000. *Digital Modulation Techniques*. Boston: Artech House.
- [101] Sklar, B., 2001. Reed-Solomon codes. URL: http://ptgmedia.pearsoncmg.com/images/art_sklar7_reed-solomon/elementLinks/art_sklar7_reed-solomon.pdf, pp. 1-33 [11/21/2017].
- [102] Chen, C.-L., and Hsiao, M.Y., 1984. Error-correcting codes for semiconductor memory applications: A state-of-the-art review. *IBM Journal of Research and Development*, 28(2), pp. 124-134.
- [103] Chen, B., Zhang, X. and Wang, Z, October, 2008. Error correction for multi-level NAND flash memory using Reed-Solomon codes. *IEEE Workshop on Signal Processing Systems*, pp. 94-99.
- [104] Bertozzi, D., Benini L., and De Micheli, G., 2005. Error control schemes for on-chip communication links: the energy-reliability tradeoff. *IEEE Transactions on Computer-Aided Design of Integrated Circuits and Systems*, 24(6), pp. 818-831,
- [105] Yang, C., Emre, Y., and Chakrabarti, C., 2012. Product code schemes for error correction in MLC NAND flash memories. *IEEE Transactions on Very Large-Scale Integration (VLSI) Systems*, 20(12), pp. 2302-2314.
- [106] Sun, Z., and Akyildiz, I.F., 2010. Magnetic induction communications for wireless underground sensor networks. *IEEE Transactions on Antennas and Propagation*, 58(7), pp. 2426-2435.
- [107] Jornet, J.M., and Akyildiz, I.F., 2012. Joint energy harvesting and communication analysis for perpetual wireless nanosensor networks in the terahertz band. *IEEE Transactions on Nanotechnology*, 11(3), pp. 570-580.
- [108] Wang, Z.L., 2008. Towards self-powered nanosystems: From nanogenerators to nano piezotronics. *Advanced Functional Materials*, 18(22), pp. 3553-3567.
- [109] Xu, S., Hansen, B.J., and Wang, Z.L., 2010. Piezoelectric-nanowire-enabled power source for driving wireless microelectronics. *Nature Communications*, 1, p. 1098.

REFERENCES (continued)

- [110] Xu, S., Qin, Y., Xu, C., Wei, Y., Yang, R., and Wang, Z.L., 2010. Self-powered nanowire devices. *Nature Nanotechnology*, 5(5), pp. 366-373.
- [111] Pech, D., Brunet, M., Durou, H., Huang, P., Mochalin, V., Gogotsi, Y., Taberna, P.-L., and Simon, P., 2010. Ultrahigh-power micrometre-sized supercapacitors based on onion-like carbon. *Nature Nanotechnology*, 5(9), pp. 651-654.
- [112] Wicker, S.B., and Bhargava, V.K., 1994. An introduction to Reed-Solomon codes. In *Reed-Solomon Codes and Their Applications*. New Jersey: IEEE Press, pp. 1-16.
- [113] Goldsmith, A., 2005. *Wireless communications*. Cambridge university press.